International Journal of Coal Geology 312 (2025) 104897

Contents lists available at ScienceDirect

International Journal of Coal Geology

journal homepage: www.elsevier.com/locate/coal

OM-hosted pore systems in Ordovician Wufeng–Silurian Longmaxi shales in Sichuan Basin SW China: Origin, gas storage, and flow behavior

Yong Ma [a,**], Omid H. Ardakani [b,e], Dahua Li [c], Jianbin Ma [a], Ningning Zhong [a], Haiping Huang [d,e,*]

[a] State Key Laboratory of Petroleum Resources and Engineering, China University of Petroleum (Beijing), Beijing 102249, PR China
[b] Natural Resource Canada, Geological Survey of Canada, Calgary, AB, Canada
[c] Key Laboratory of Shale Gas Exploration, Ministry of Natural–Resources, Chongqing Institute of Geology and Mineral Resources, Chongqing 401120, PR China
[d] School of Geosciences, Yangtze University, Wuhan 430100, Hubei, PR China
[e] Department of Earth, Energy, and Environment, University of Calgary, Calgary T2N 1N4, Canada

ARTICLE INFO

Keywords:
Organic matter porosity
Alginite
Graptolite
Pyrobitumen
Fecal pellets
Permeability

ABSTRACT

This study provides an extensive investigation of the origin, morphological evolution, pore structure, and flow behavior of organic matter (OM)-hosted pore systems in the overmature Wufeng–Longmaxi (W–L) shales of the Sichuan Basin, SW China, with implications for shale gas storage and production. Eleven core samples from the Wufeng and Longmaxi formations, spanning a wide range of total organic carbon (TOC) content (0.47–5.48 wt%) but consistently high thermal maturity (EqVRo 3.89–4.20 %), were analyzed using a combination of geochemical analyses, optical microscopy, high-resolution scanning electron microscopy (SEM), three-dimensional focused ion beam-SEM (FIB-SEM) reconstructions, energy dispersive spectroscopy (EDS), and Navier–Stokes-based pore-scale permeability simulations. The OM assemblage comprises pyrobitumen, alginite, graptolites, and fecal pellets, each contributing distinct pore-forming pathways controlled by original ultrastructure, depositional redox conditions, and subsequent diagenetic mineralization. Alginite preserves sponge-like cellular ultrastructures, yielding highly connected macropore networks (> 50 nm), with the highest porosity (> 10 %) and permeability (> 15 μD), representing the most efficient storage and flow pathways. Pyrobitumen develops irregular shrinkage pores and microfracture networks during thermal cracking, producing moderate porosity (4–13 %) and permeability (~ 0.75 μD), with framboidal pyrite stabilizing pore structures against compaction. Fecal pellets, stabilized by early phosphatization through apatite and fluorapatite precipitation, retain isotropic nanoporous frameworks (40–160 nm) with consistent porosity (~ 5 %) and permeability (~ 0.8 μD). In contrast, graptolites display poorly connected cortical fibril-aligned nanometer-sized pores (< 20 nm), contributing minimally to storage (porosity <0.6 %) and permeability (< 0.35 μD). Pore size distribution analysis reveals that alginite and pyrobitumen host the largest connected pores, whereas graptolites and fecal pellets are dominated by isolated, ultrafine structures. Diagenetic mineralization emerges as a critical factor in pore preservation, with apatite and pyrite reinforcing nanoporous networks against mechanical collapse. Furthermore, depositional conditions such as water column stratification, nutrient influx, microbial restructuring, and limited degradation of fecal aggregates facilitated OM preservation, leading to the formation of stable nanoporosity critical for long-term gas storage and migration. Integrated FIB-SEM reconstructions and flow simulations establish a hierarchical permeability ranking of alginite > pyrobitumen ≈ fecal pellets > > graptolites, underscoring the significant role of OM type and diagenetic evolution governing shale reservoir quality. These findings highlight that OM composition and its diagenetic trajectory, rather than TOC or maturity alone, are the primary controls on pore network evolution, reservoir heterogeneity, and shale gas productivity in overmature marine systems such as the Wufeng–Longmaxi Formation.

* Corresponding author at: School of Geosciences, Yangtze University, Wuhan 430100, Hubei, PR China.
** Corresponding author.
E-mail addresses: mayong@cup.edu.cn (Y. Ma), huah@ucalgary.ca (H. Huang).

https://doi.org/10.1016/j.coal.2025.104897
Received 26 June 2025; Received in revised form 2 November 2025; Accepted 2 November 2025
Available online 4 November 2025

1. Introduction

Organic matter (OM)-hosted pores are a critical component of porosity in organic-rich shales, directly influencing both hydrocarbon production and the emerging application of carbon capture and storage (CCS) (Curtis et al., 2012; Loucks et al., 2012; Mastalerz et al., 2013; Reed et al., 2020). These nanometer-scale pores, according to IUPAC pore size classification (Sing, 1985), originate from multiple processes, including the thermal transformation of kerogen and solid bitumen and the preservation of biogenic ultrastructures, serving as both storage sites and conduits for fluid transport in overmature shale systems (Ko et al., 2016; İnan et al., 2018). The type, origin, and maturity of OM are among major drivers of determining pore development, morphology, and connectivity (Loucks et al., 2009; Ardakani et al., 2018; Katz and Arango, 2018; Teng et al., 2022; Lis et al., 2025; Shao et al., 2025), underscoring the heterogeneity in OM-hosted pore systems.

Among OM types, high thermal maturity solid bitumen especially pyrobitumen that form at advanced thermal maturity (Ro $\geq$ 1.5 %; Mastalerz et al., 2018) has been widely recognized as a dominant pore-hosting phase (Curtis et al., 2012; Zargari et al., 2015; Teng et al., 2022). Formed from the in-situ thermal cracking of migrated oil (Mastalerz et al., 2018; Gao et al., 2020), pyrobitumen typically develops larger, more spherical, and well-connected pores compared to other OM types (Ma et al., 2016; Teng et al., 2022). İnan et al. (2018) further demonstrated that solid bitumen porosity is substantially enhanced during gas expulsion, especially in quartz-rich shales that resist compaction and preserve pore structures (e.g., Knapp et al., 2020). In contrast, graptolites and other marine zooclasts such as chitinozoans, scolecodonts, and conodont elements, contribute elongated, fibrillar nanopores that are structurally aligned but poorly connected, often resulting in low permeability and limited contribution to fluid storage (Ma et al., 2016; Cao et al., 2020; Shi et al., 2020; Xu et al., 2020). While these aligned pores may enhance directional flow under certain conditions, their overall contribution to effective porosity remains minimal due to mineral infill and poor interconnectivity.

Other OM types such as alginite and fecal pellets add further complexity to OM heterogeneity (Slatt and O'Brien, 2011; Loucks et al., 2012; Löhr et al., 2015; Hackley and Cardott, 2016). Alginite retains its original cellular framework, forming high biogenic primary porosity with abundant intergranular pores that evolve into well-connected OM-hosted networks during maturation, thus providing both significant storage capacity and isotropic flow pathways (Löhr et al., 2015; Ma et al., 2018). In contrast, fecal pellets exhibit moderate porosity and often contain early diagenetic apatite, reflecting microbial activity and phosphogenesis that enhance organic preservation and contribute to well-preserved nanopore networks (Hirschler et al., 1990; Krajewski, 2013; MacIver et al., 2021).

The Upper Ordovician Wufeng and the Silurian (Llandovery) Longmaxi formations in the Sichuan Basin, SW China, serve as excellent case studies for OM-hosted pore evolution, given their high thermal maturity (EqVRo >2.6 %) and high TOC content (> 2.0 %) (Zou et al., 2015; Teng et al., 2022). Deposited under episodically anoxic conditions in a semi-closed marine basin, these graptolite-rich black shales accumulated OM through high biological productivity and periodic volcanic ash influx rich in nutrients (N, P, Si, Fe, Al), which further promoted OM production, preservation, and diversity (Zhang et al., 2020; Qiu et al., 2022). Consequently, these formations host complex OM assemblages, including pyrobitumen, alginite, graptolites, and fecal pellets, each contributing uniquely to the pore systems.

While early studies heavily relied on 2D SEM imagery, recent advances in broad ion beam polishing and SEM (BIB-SEM) / liquid metal injection-BIB-SEM (LMI-BIB-SEM), FIB-SEM 3D reconstructions and Navier–Stokes-based permeability modeling have enabled detailed quantitative insights into nanometer-scale pore geometries, interconnectivity, and directional permeability (Loucks and Reed, 2014; Zhu et al., 2021; Liu et al., 2022; Klaver et al., 2024). These high-resolution techniques allow precise quantification of OM surface porosity, pore size distribution (PSD), and permeability tensors across OM types.

Recognizing the differences in OM-hosted pore structures is crucial for accurately predicting pore network evolution and optimizing shale reservoirs for both hydrocarbon production and long-term CO_2 storage applications (Ma et al., 2018; Wang and Jin, 2019; Garum et al., 2020; Wang and Cheng, 2023; Wang et al., 2023). Understanding these distinctions is equally critical for evaluating hydrocarbon migration pathways, identifying sweet spots, and improving resource recovery in overmature shales (Ma et al., 2025a). However, a significant knowledge gap persists due to the absence of systematic comparisons among macerals under consistent maturity and depositional conditions.

This study will address this gap by integrating organic petrology, 3D pore network reconstruction, and directional flow simulations of overmature organic-rich shale units, Wufeng–Longmaxi (W–L) shales, in Sichuan Basin, SW China to investigate, (1) the morphology and spatial distribution of dominant OM types; (2) quantify OM-hosted porosity and directional permeability; (3) link pore evolution to depositional and diagenetic processes; and (4) assess the relative contributions of each OM maceral to hydrocarbon storage and fluid flow. By clarifying the functional roles of OM-hosted pore systems, particularly those developed in pyrobitumen and other overmature macerals, this work offers new insights into shale gas system behavior and supports more effective exploration and production strategies in deep marine shale plays as well as CCS projects.

2. Geological setting and analytical methods

2.1. Geological setting

During the early to middle Paleozoic, tectonic activity driven by the collision between the Yangtze and Cathaysia Blocks led to the formation of a shelf basin on the southern Yangtze Block (Su et al., 2009). By the Late Ordovician, this basin had evolved into a continental shelf environment, bounded by the Qianzhong, and Xuefeng uplifts (Fig. 1A). The transition from an open marine setting in the Early to Middle Ordovician to a more restricted shelf during the Late Ordovician established a broad, low-energy, undercompensated, and anoxic depositional environment conducive to OM preservation (Liu et al., 2021).

Two major global marine transgression events in the Late Ordovician and early Silurian (Llandovery) further enhanced anoxic conditions. Rising sea levels expanded deep-water environments, and high surface productivity fueled by nutrient-rich waters led to the accumulation of planktonic organisms such as algae, radiolarians, and graptolites (Nie et al., 2019). These biogenic particles, along with clay and organic detritus, settled as marine snow on the seafloor, forming thick deposits of organic-rich black shales. These conditions resulted in the widespread development of the Upper Ordovician Wufeng Formation and the Silurian (Llandovery) Longmaxi Formation within a muddy semi-deep shelf setting (Zou et al., 2015; Wu et al., 2019). For the two wells (YC4 and QY1) located on the southeastern margin of the Sichuan Basin, the W–L black shales experienced a maximum burial depth of approximately 5100 m, followed by continuous uplift of about 4300 m since the Middle Jurassic (Tang et al., 2021). Currently, in the Sichuan Basin, the W–L black shales, enriched in graptolites, biogenic silica, and carbonates, exhibit TOC contents of 2–11 wt%, equivalent vitrinite reflectance (EqVRo) values of 2.6–4.29 %, and cumulative thicknesses of 20–80 m, forming high-quality source rocks for shale gas exploration (Zou et al., 2015; Luo et al., 2016; Ma et al., 2016; Qiu et al., 2022).

2.2. Sample collection and preparing

Fig. 1A shows the locations of the two studied wells: YC4, near the depositional center with ~100 m of Longmaxi Formation, and QY1, with a reduced thickness of ~40 m. Eleven core samples were collected from depths ranging 642.7–762.9 m (YC4 well) and at 798.8 m (QY1 well).

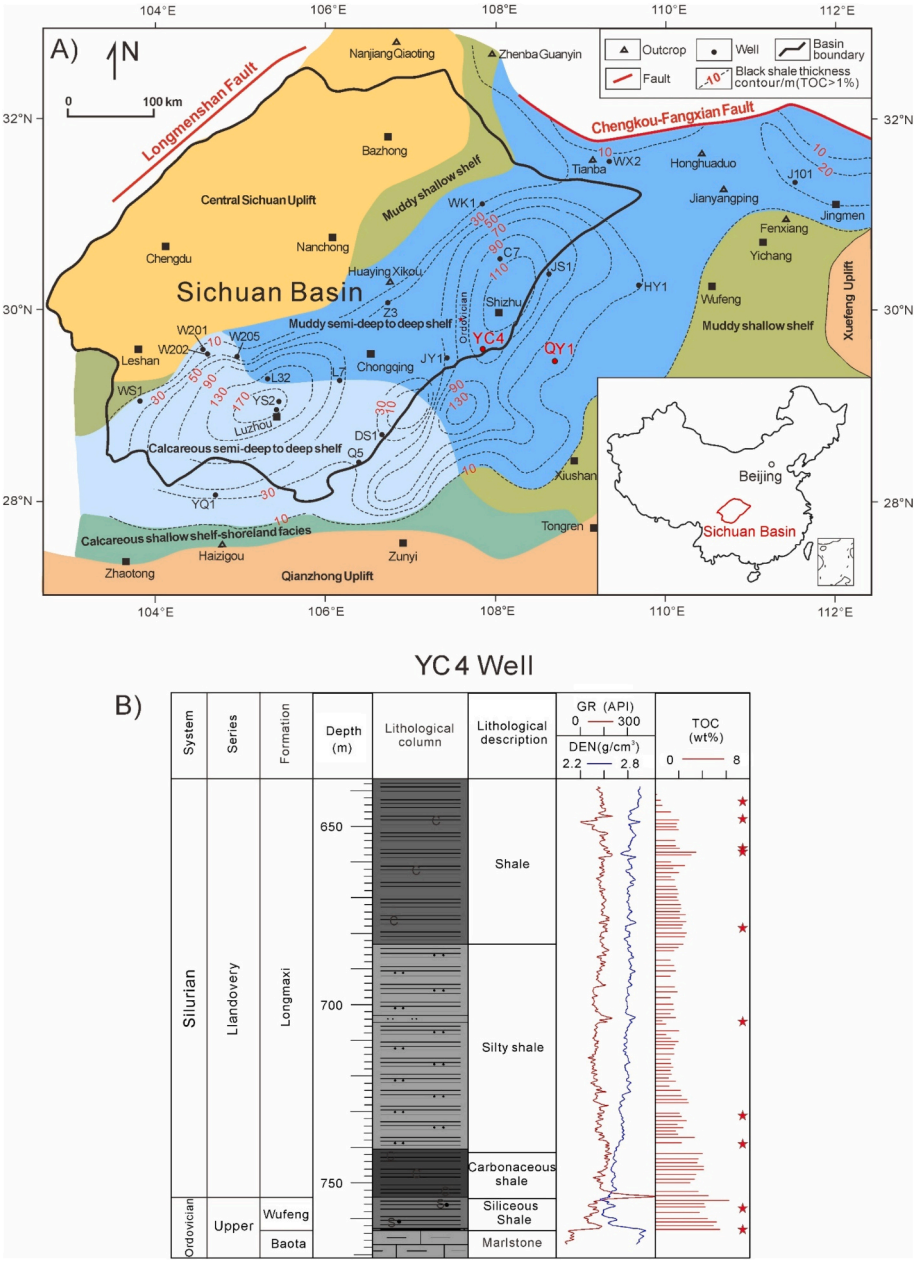

Fig. 1. (A) Location of the Sichuan Basin and adjacent regions, showing lower Longmaxi Formation facies (modified from Zou et al., 2015). (B) Stratigraphic column of the YC4 well, including lithology, logging curves, and TOC content data. Red stars mark the sampled intervals analyzed in this study. (For interpretation of the references to colour in this figure legend, the reader is referred to the web version of this article.)

These samples include siliceous shale, carbonaceous shale, and silty shale. Fig. 1B details the stratigraphy and log data of the YC4 well, highlighting organic-rich intervals primarily concentrated in the black shale sections of the Wufeng and lower Longmaxi formations.

Core samples were cut perpendicular to bedding plane. One polished section was used for optical microscopy, and another for SEM and FIB-SEM imaging. Remaining material was pulverized to ≤60 mesh (250 μm) for TOC analysis. All geochemical and imaging analyses (except organic petrology) were performed at the National Key Laboratory of Petroleum Resources & Engineering, China University of Petroleum--Beijing. Organic petrology analyses were conducted at the Geological Survey of Canada in Calgary.

2.3. Total organic carbon (TOC) content

Crushed shale samples were first treated to remove inorganic carbon before TOC analysis. Each powdered sample was placed in a porcelain crucible and treated with 12.5 % hydrochloric acid (HCl by volume) on an electric hot plate maintained at 60–80 °C for approximately three hours to dissolve carbonate minerals. After acid treatment, the samples were rinsed multiple times with distilled water to eliminate residual HCl, then dried in an oven at 60–80 °C until completely free of moisture. The decarbonated samples were subsequently analyzed for TOC content using a LECO CS230 carbon and sulfur analyzer, which combusts the sample in a high-temperature furnace and quantifies carbon via infrared detection. This method follows the Chinese Standard GB/T 19145–2022, with an analytical precision of ±0.5 wt%.

2.4. Organic petrography

Polished shale slabs were examined under a Zeiss Axioimager II microscope system equipped with incident white light and ultraviolet

(UV) illumination. Reflectance measurements were acquired using Diskus Fossil software (Hilgers Technisches Buero) under oil immersion conditions with a 50× objective lens. The analysis followed the standard procedures outlined by ASTM for reflectance measurement of solid bitumen. For calibration, an yttrium–aluminum–garnet (YAG) standard with a known reflectance values of 0.906 % and 0.001 % was used. Measured random bitumen reflectance (BRo) values were converted into EqVRo to approximate thermal maturity, using the equation by Wang et al. (2020):

$$EqVRo = 1.125 \times BRo - 0.2062.$$

2.5. Scanning electron microscopy (SEM)

Shale fragments (~1 cm^2) were mechanically pre-polished using a Leica EM TXP target surfacing system to ensure flat surfaces suitable for high-resolution imaging. To enhance surface quality and pore visibility, samples were further processed via ion beam milling using a Leica EM RES102 system at 3 kV for 6–10 h. Milled specimens were affixed onto SEM stubs with carbon adhesive and coated with a thin layer of carbon to provide electrical conductivity. Imaging was performed with a Zeiss Crossbeam 540 FIB-SEM, allowing nanoscale visualization of shale textures, pores, and organic matter. In addition, energy-dispersive X-ray spectroscopy (EDS) using Bruker Quantax detectors was employed to identify and quantify mineral phases, particularly for uncertain or fine-grained constituents.

2.6. FIB-SEM 3D reconstruction and permeability simulation

After SEM screening, regions rich in macerals such as graptolite and pyrobitumen were selected for three-dimensional analysis using focused ion beam-scanning electron microscopy (FIB-SEM). The analysis involved sequential milling and imaging of cross-sectional slices using a gallium ion beam. A protective platinum layer was first deposited over the region of interest to prevent beam damage. The ion and electron beams were aligned at a 54° angle to optimize sectioning and imaging. FIB milling removed thin slices (~10 nm each) across the target area, with SEM imaging following each cut. This process was repeated over 900 cycles to generate a high-resolution image stack of the shale's microstructure.

The resulting image sequences were processed using Avizo® Fire 9.0.1 software to reconstruct three-dimensional distribution of pores, minerals, and OM. Image segmentation was conducted based on gray-scale contrast to distinguish features with overlapping densities. Using Avizo's finite element modeling tools, simulations were run to estimate anisotropic absolute permeability of the interconnected pore networks in three orthogonal directions. These simulations applied a simplified Navier–Stokes equation to model steady-state, laminar flow of water under differential pressure conditions (1.3×10^{-5} Pa upstream vs. 1.0×10^{-5} Pa downstream), capturing flow heterogeneity based on pore network structure (Peng et al., 2014; Callow et al., 2018, 2020; Ma et al., 2025b). Both drilling and uplift following the maximum burial depth of these shales can significantly alter the temperature and hydrodynamic pressure, which in turn may greatly affect the physical properties of the rock. This is a complex process that is difficult to fully reconstruct. Therefore, permeability simulations were conducted under identical conditions to ensure the comparability and reliability of the flow behavior among different macerals.

3. Results

3.1. Maturity, and organic richness of Wufeng–Longmaxi shales

Table 1 presents geochemical and stratigraphic data for 11 shale samples from a vertical profile spanning the W–L formations. The Longmaxi section includes eight samples (642.7–738.7 m), while three deeper samples (756.7–798.8 m) represent the Wufeng Formation. The TOC content ranges from 0.47 to 5.48 wt%, with higher values in deeper Wufeng samples. Mean TOC content is 4.1 wt% in Wufeng and 1.9 wt% in Longmaxi. EqVRo values derived from pyrobitumen (3.89–4.20 %) are consistently high and align closely with those obtained from graptolite reflectance (3.65–4.29 %) for three Longmaxi shale samples from the YC4 well, at burial depths of 656.2–745.3 m (Luo et al., 2016), indicating an overmature thermal regime associated with dry gas windows. A clear stratigraphic trend of increasing TOC content with depth is observed, particularly across the W–L boundary.

Table 1
List of analyzed samples with depth, formation, TOC contents, and EqVRo.

Sample ID	Series	Formation	Depth (m)	TOC (wt %)	EqVRo (%)
YC4–2	Llandovery	Longmaxi	642.7	0.47	4.20
YC4–7		Longmaxi	648.2	2.03	4.13
YC4–15		Longmaxi	656.2	2.08	4.02
YC4–16		Longmaxi	657.2	3.47	
YC4–38		Longmaxi	678.6	2.27	
YC4–59		Longmaxi	704.4	0.63	4.09
YC4–82		Longmaxi	730.5	2.09	4.16
YC4–91		Longmaxi	738.7	2.23	4.05
YC4–105	Upper Ordovician	Wufeng	756.7	4.25	4.09
YC4–110		Wufeng	762.9	5.48	4.13
QY1–1		Wufeng	798.8	2.64	3.89

3.2. Morphological characteristics and distribution of organic matter in the Wufeng–Longmaxi shales

Fig. 2 presents organic petrology photomicrographs of the W–L shales under incident white light with oil immersion, highlighting the diversity, morphology, and spatial distribution of key OM components—namely alginite, graptolites, fecal pellets, and pore-filling pyrobitumen. These OM components significantly influence porosity, permeability, and hydrocarbon storage.

At advanced thermal maturity, alginite (algal fragments) is observed lying parallel to bedding (Fig. 2A–B) and has undergone in situ transformation into pyrobitumen. This pyrobitumen occurs both as dispersed particles within the matrix and as pore-filling accumulations, particularly between clay platelets and within intergranular pores of silt-rich laminae (Fig. 2A, B, E, F). During later stages of maturation, the original bitumen experienced secondary cracking, resulting in the formation of pyrobitumen. It is frequently associated with pyrite framboids, suggesting post-migration emplacement under reducing conditions (Fig. 2E–F).

Graptolites, a dominant zooclast component, are abundant and typically aligned with bedding (Fig. 2C). The graptolite rhabdosomes are well preserved, showing granular textures and prominent cortical fibrils visible under both plane- and cross-polarized light (Fig. 2D), confirming their bi-reflectance character and structural granularity.

Fecal pellets and possible phosphate nodules are also present (Fig. 2G–H). These exhibits elliptical to circular morphologies and homogeneous internal textures, suggesting they were formed by microbial activity. Some display concentric zonation (Fig. 2H), a characteristic feature of phosphatic nodules.

Fig. 3 and Table 2 present the relative abundance and distribution of major macerals, pyrobitumen, graptolite, alginite, and fecal pellets, in seven shale samples (YC4–2 to YC4–110) from the YC4 well, based on SEM image analysis. Total OM surface coverage varies widely, from 0.17 % in YC4–2 to 12.53 % in YC4–110, reflecting substantial heterogeneity in OM content and composition. Pyrobitumen dominates all samples, particularly those with low total OM content. In YC4–2, for example, pyrobitumen makes up 0.13 % of the 0.17 % total OM, accounting for over 75 % of the organic area. Graptolite is the only other identifiable OM type (0.05 %), while alginite and fecal pellets are absent. In samples with moderate OM content, such as YC4–16 (5.26 %),

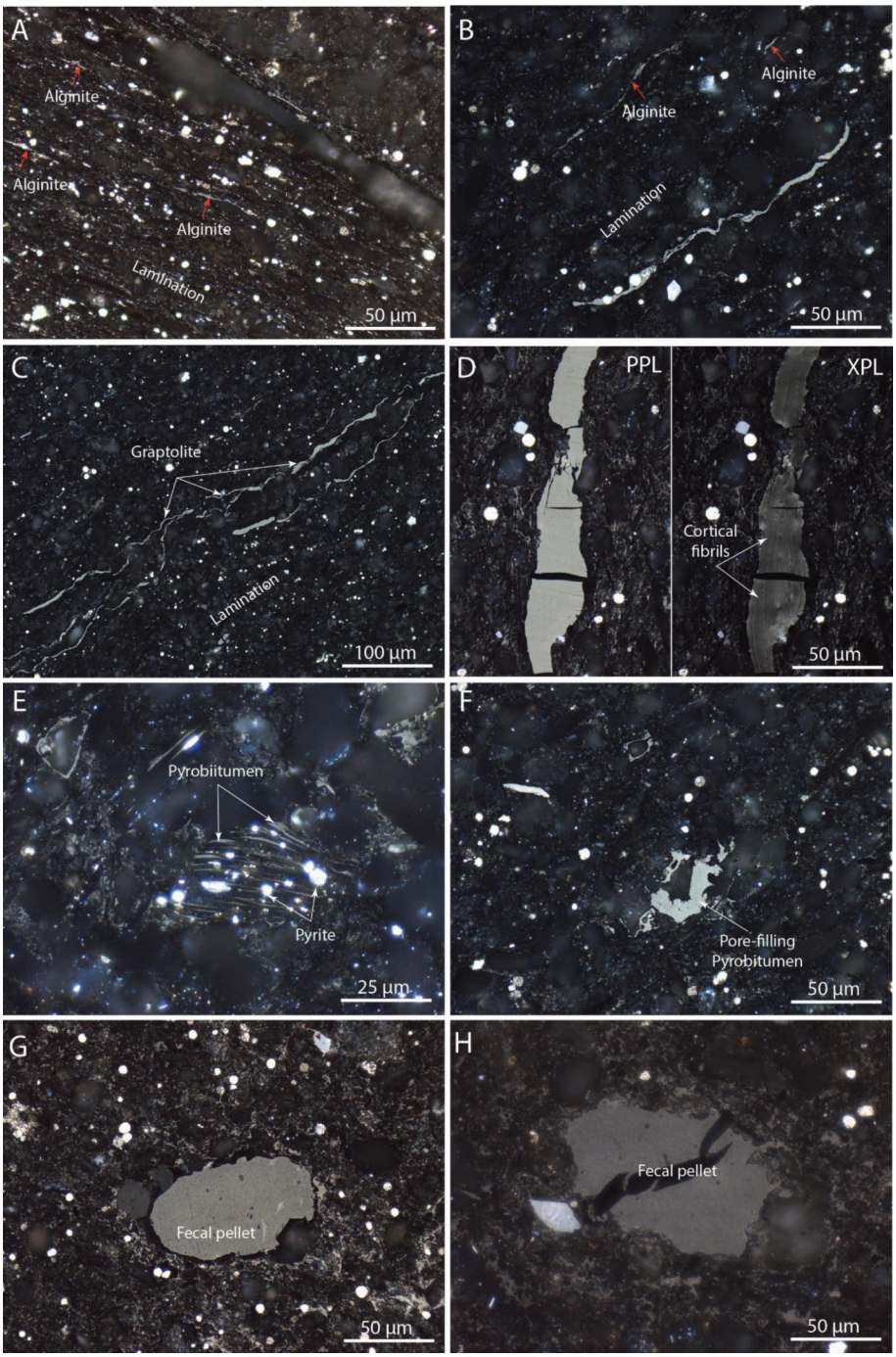

Fig. 2. Organic petrology photomicrographs of W–L shales under white incident light with oil immersion, illustrating key organic components. (A) Alginite parallel to the bedding, in-situ transformed to pyrobitumen, Sample YC4–15. (B) Alginite in-situ transformed into pyrobitumen in a fine-grain shale matrix, Sample YC4–15. (C) Graptolite aligned with lamination, Sample YC4–15. (D) Cortical fibrils within a bandage ultrastructure under reflected plane polarized light (PPL) and cross polarized light (XPL), Sample YC4–109. (E) Pyrobitumen filled pores between clay platelets; pyrite framboids visible in intergranular pores (Sample YC4–15). (F) Pore-filling pyrobitumen, Sample YC4–15. (G-H) Elliptical fecal pellets (G) and phosphatic nodules (H) embedded in the shale matrix, Sample YC4–105.

YC4–38 (4.66 %), and YC4–91 (10.82 %), pyrobitumen was the dominant maceral (4.30–9.57 %), with minor contributions from graptolite (0.26–1.02 %), and occasional occurrences of alginite or fecal pellets. The most compositionally diverse samples were YC4–105 and YC4–110. In YC4–105, pyrobitumen (4.79 %) coexists with nearly equal amounts of alginite (1.14 %) and graptolite (1.14 %), alongside minor fecal pellets (0.23 %). YC4–110 exhibits the highest total OM content (12.53 %) and the greatest proportion of graptolite (3.68 %) and fecal pellets (2.75 %), with additional contributions from pyrobitumen (5.78 %) and alginite (0.32 %).

3.3. OM-hosted pore system in the Wufeng–Longmaxi shales

Fig. 4 presents high-resolution SEM images highlighting the contrasting pore architectures of alginite and pyrobitumen in the W–L shales from the YC4 well, which are critical to understanding OM-hosted porosity and shale reservoir quality. Fig. 4A–D focus on alginite from sample YC4–105. In Fig. 4A, an alginite fragment lies parallel to bedding and is characterized by well-preserved internal ultrastructures. Fig. 4B shows an enlarged region featuring elongated, directionally aligned biological cavities, indicative of preserved algal cellular ultrastructure.

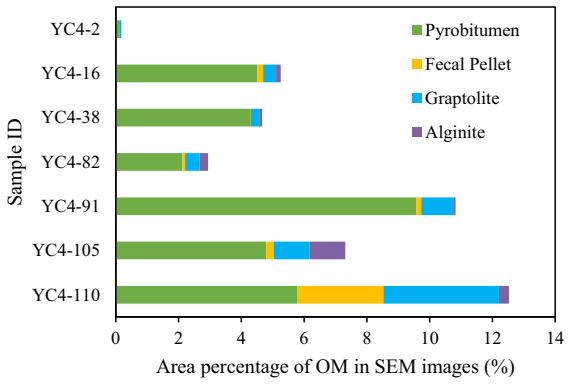

Fig. 3. Bar chart showing relative area percentages of three main OM components based on SEM image analysis.

Fig. 4C further enlarges the ultrastructure, revealing densely packed oval to elliptical pores, likely corresponding to original algal vesicles and putative cellular ultrastructures. Fig. 4D offers a close-up view showing highly connected, submicron to ~1 μm pores, forming a network of primary biogenic porosity. This type of porosity is interpreted as a possible remnant of the original organic ultrastructure; however, its biogenic origin remains uncertain at this level of thermal maturity.

Fig. 4E–F display the internal pore system of pyrobitumen in sample YC4–82. Fig. 4E reveals a pore-filling pyrobitumen cluster with heterogeneous pore distribution—rounded pores dominate the central region, while the upper left is noticeably pore-depleted, possibly due to thermal collapse or differences in precursor OM composition. Fig. 4F shows a FIB cross-section of the same pyrobitumen cluster, exposing an array of thermally induced, rounded to sub-rounded cavities. These are interpreted as secondary pores generated during hydrocarbon cracking, indicating that pyrobitumen contributes significantly to porosity in overmature shales, particularly during catagenesis.

Fig. 5 displays SEM images illustrating the morphological complexity and pore structure of pore-filling pyrobitumen in the W–L shales, underscoring its heterogeneous contribution to shale reservoir porosity. Fig. 5A–B (Sample YC4–15) show pyrobitumen infilling intergranular pores between angular quartz grains. The pyrobitumen appears irregular and discontinuous, forming void-filling structures. At higher magnification (Fig. 5B), the internal pore system reveals considerable variability in size and shape, with smaller, more interconnected pores coexisting alongside larger, isolated voids. This contrast reflects differential thermal cracking, redistribution during migration, and diagenesis.

Fig. 5C–D (Sample YC4–82) depict pyrobitumen embedded within clay-rich laminae and closely associated with pyrite framboids. Fig. 5C shows elongated strands of pyrobitumen aligned with clay platelets, suggesting migration along mechanical discontinuities. In Fig. 5D, the pyrobitumen exhibits abundant nanoscale pores, indicating partial preservation of pyrobitumen-hosted porosity even after thermal degradation. The presence of aligned clay ultrastructures also suggests pore system anisotropy and directional flow pathways.

Fig. 5E–F further highlight the relationship between pyrobitumen and mineral phases. In Fig. 5E, pyrobitumen occurs adjacent to densely packed pyrite framboids, typical of a reducing depositional

Table 2
Area percentages of total organic matter, pyrobitumen, graptolites, and fecal pellets as identified from SEM image analysis.

Sample ID	Total statistical view area (μm^2)	Area percentage of area (%)				
		Total Organic Matter	Pyrobitumen	Alginite	Graptolite	Fecal pellets
YC4–2	1,236,049	0.17	0.13	0	0.05	0
YC4–16	1,742,118	5.26	4.51	0.15	0.41	0.19
YC4–38	1,955,011	4.66	4.30	0.09	0.26	0.01
YC4–82	1,840,643	2.95	2.12	0.27	0.46	0.09
YC4–91	2,036,590	10.82	9.57	0.07	1.02	0.16
YC4–105	714,804	7.31	4.79	1.14	1.14	0.23
YC4–110	793,384	12.53	5.78	0.32	3.68	2.75

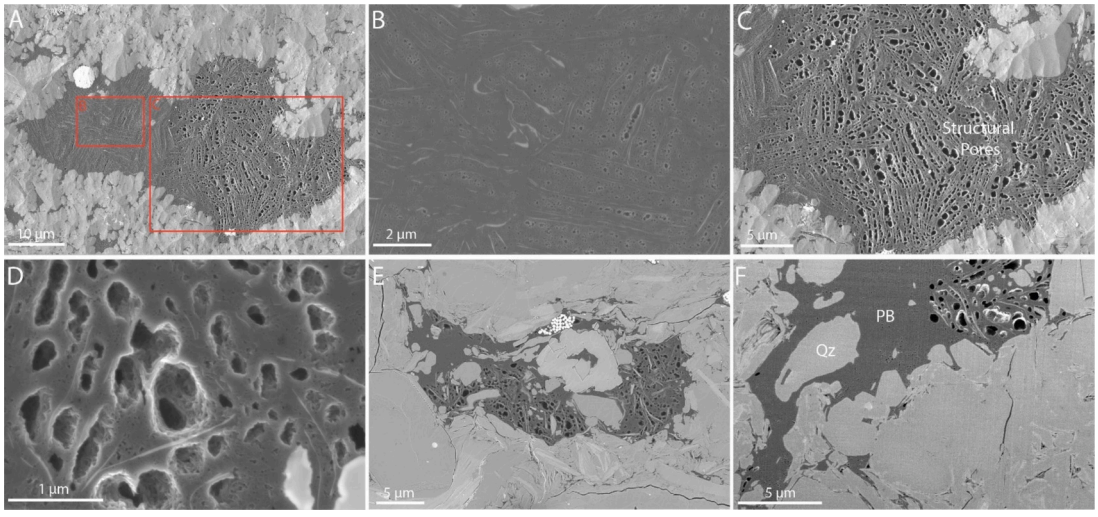

Fig. 4. SEM images showing the morphology and pore structure of alginite and pyrobitumen. (A) Alginite oriented parallel to bedding (Sample YC4–105). (B) Enlarged view of (A) displaying directionally aligned pores along the alginite structure. (C) Magnified view of (A) showing well-developed pores distributed along the wall of a biological cavity within the alginite structure. (D) Close-up of alginite highlighting its porous architecture (Sample YC4–105). (E) Pore-filling pyrobitumen with heterogeneous pore distribution—dense, rounded pores dominate except in the pore-depleted upper left corner (Sample YC4–82). (F) FIB cross-section of (E) revealing internal heterogeneity of the pyrobitumen-hosted pore system. Qz = quartz, PB = Pyrobitumen.

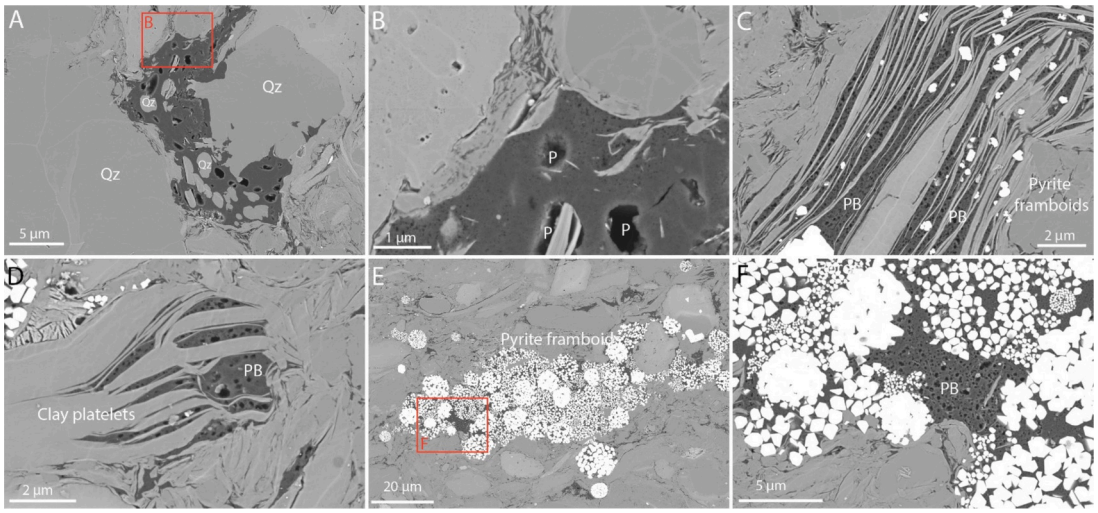

Fig. 5. SEM images showing the morphology and pore characteristics of pyrobitumen in W–L shales. (A) Pyrobitumen filling intergranular pores between quartz grains (Sample YC4–15). (B) Enlarged view of (A), revealing pores of variable sizes within the pyrobitumen matrix. (C) Pyrobitumen and pyrite co-occurring within clay platelets (Sample YC4–15). (D) Porous pyrobitumen embedded in clay platelets (Sample YC4–82). (E) Layered pyrite framboids adjacent to pyrobitumen (Sample YC4–82). (F) Close-up of porous pyrobitumen situated between pyrite crystals. Qz = Quartz, P=Pores, PB = Pyrobitumen.

environment. A close-up in Fig. 5F reveals porous pyrobitumen matrices tightly interwoven with pyrite aggregates. These mineral-organic interfaces likely influence pore preservation. They may enhance pore stability through mechanical shielding or reduce pore space due to overgrowth and compaction.

Fig. 6 presents a series of high-resolution SEM images that detail the internal ultrastructure and pore development of graptolites, underscoring their contribution to anisotropic porosity in the W–L shales. Fig. 6A (Sample YC4–105) shows a graptolite fragment aligned with bedding, exhibiting clear lamination and a well-defined boundary with the surrounding shale matrix. The red-boxed area is enlarged in Fig. 6B, which reveals cortical band ultrastructure composed of concentric cortical fibrils, outlined by yellow dashed lines. This layered arrangement, biologically inherited from the original organism, provides a framework for porosity retention even after thermal alteration.

Fig. 6C exhibits a closer view of the cortical bands, where nanometer-scale pores are preserved between fibril layers. These inter-fibril voids represent primary biogenic porosity, directly linked to the original tissue morphology. In Fig. 6D (Sample YC4–82), similar concentric fibrils are seen, partially disrupted by a microfracture, indicating that mechanical deformation during diagenesis may enhance pore connectivity and extend fluid pathways.

Fig. 6E and F (Sample QY1–1) highlight a different pore style; elongated, fracture-like pores embedded within the cortical fibril framework. Fig. 6E shows aligned, narrow voids consistent with thermal cracking or stress-induced pore generation, while Fig. 6F provides a high-magnification view, revealing submicron-scale pores (< 500 nm) that run parallel to the fibrils. These pores are likely secondary in origin but maintain structural coherence due to the rigid bandage framework, thus supporting anisotropic, directionally biased fluid flow within the graptolite bodies.

Fig. 7 displays SEM images that characterize the morphology, internal ultrastructure, and pore systems of fecal pellets in the W–L shales, highlighting their role as mineralized, organic-rich microfacies contributing to shale reservoir porosity and hydrocarbon storage. Fig. 7A–B (Sample YC4–82) show an elliptical fecal pellet embedded in a

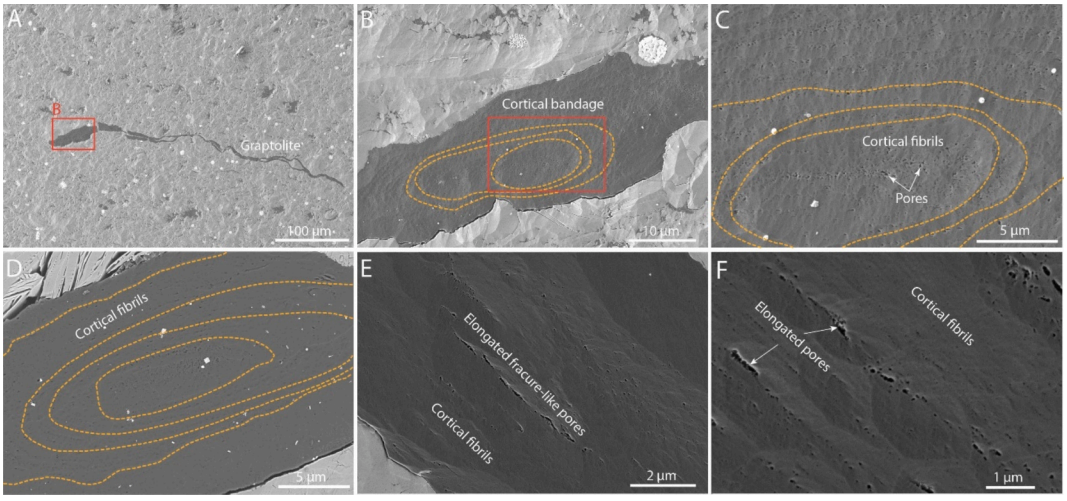

Fig. 6. SEM images illustrating the morphology and pore systems of graptolites (A–F) in W–L shales. (A) Flattened graptolite exhibiting fine lamination (Sample YC4–105). (B) Enlarged view of (A), highlighting the girdle-like arrangement of cortical fibrils. (C) Close-up of the cortical bandage in (B), showing nanometer-scale pores between fibrils. (D) Girdle ultrastructure of cortical fibrils in another graptolite sample (Sample YC4–82). (E) Fracture-like, elongated pores between cortical fibrils within a bandage ultrastructure (Sample QY1–1). (F) Enlarged view of (E), emphasizing the elongated inter-fibril pore geometry.

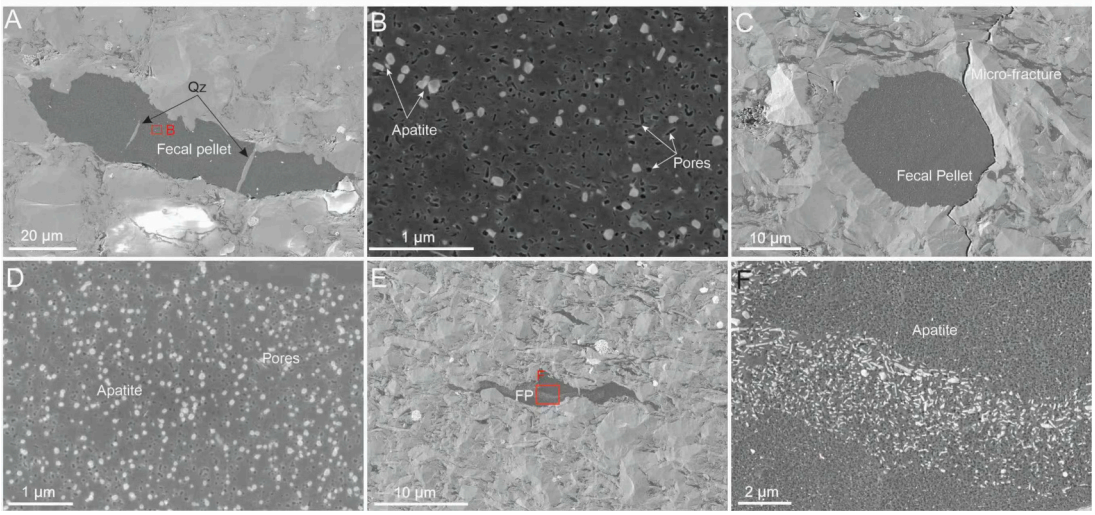

Fig. 7. SEM images showing the morphology and pore system of fecal pellets in W–L shales (A–F). (A) Elliptical fecal pellet aligned parallel to bedding, containing quartz inclusions (Sample YC4–82). (B) Enlarged view of (A), revealing apatite grains and irregular pores within the pellet. (C) Circular fecal pellet oriented parallel to bedding. (D) Enlarged view of (C), showing granular apatite and irregular internal porosity (Sample YC1–110). (E) Elongated fecal pellet parallel to bedding (Sample YC4–110). (F) Enlarged view of (E), highlighting elongated columnar apatite crystals within the porous pellet matrix. FP=Feldspar.

quartz-rich matrix and oriented parallel to bedding, suggesting deposition in a low-energy, anoxic environment. The pellet appears compact and well-defined. Fig. 7B (higher magnification view) reveals abundant submicron-scale pores distributed irregularly across the matrix, along with dispersed bright inclusions of apatite, likely a result of microbial activity and early diagenetic mineralization. These features contribute to nanoporous textures that may contribute to hydrocarbon retention.

Fig. 7C–D (Sample YC4–110) illustrate a more rounded fecal pellet, aligned with bedding and intersected by microfractures, which could enhance pore connectivity. Fig. 7D, a high-magnification view, shows

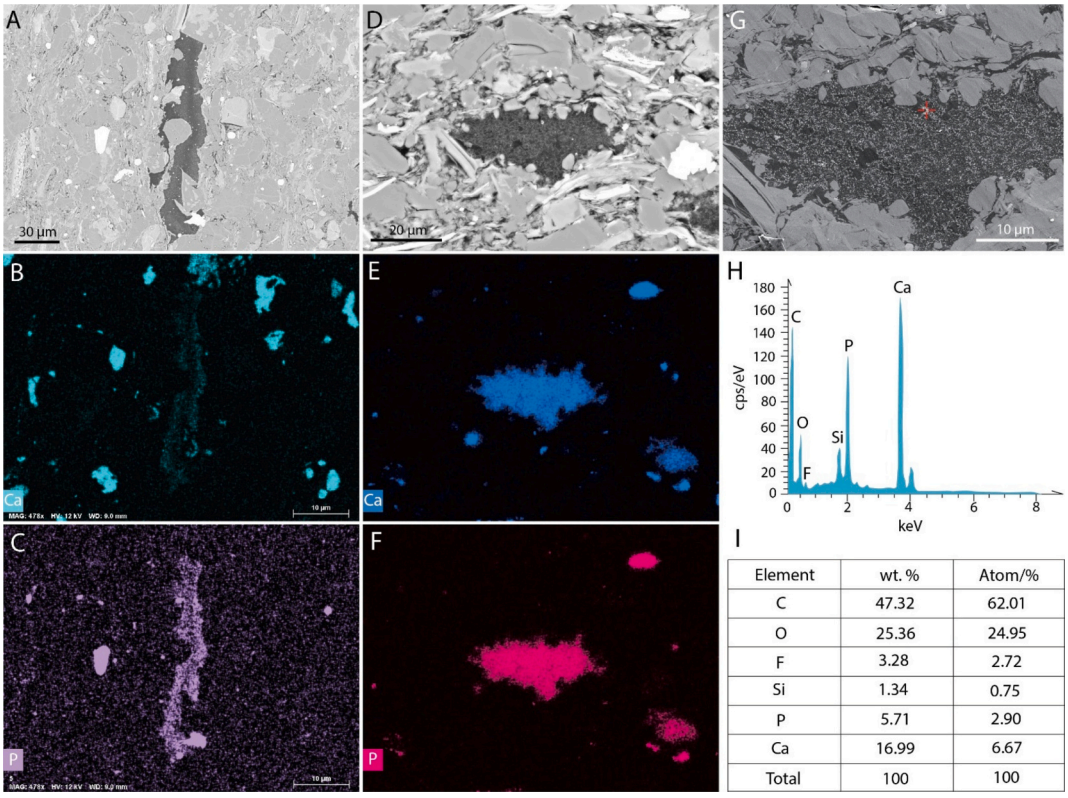

Element	wt. %	Atom/%
C	47.32	62.01
O	25.36	24.95
F	3.28	2.72
Si	1.34	0.75
P	5.71	2.90
Ca	16.99	6.67
Total	100	100

Fig. 8. Energy dispersive X-ray spectroscopy (EDS) analyses of calcium- and phosphate-rich fecal pellets in the W–L shales. (A) SEM image of an elongated fecal pellet aligned parallel to bedding (Sample YC4–16). (B-C) EDS elemental maps showing a weak calcium signal but strong phosphate distributions within the pellet. The Ca-rich areas represent calcite. (D) SEM image of an elliptic fecal pellet (Sample YC4–110). (E–F) EDS spectrum and corresponding calcium and phosphate elemental composition of apatite in (D). (G) Enlarged view of (D), highlighting apatite crystals. (H-I) EDS analyses showing the elemental composition of apatite in the pellet, as the red cross shown in (G). Note: The minimum spatial resolution for SEM-EDS is ~1 μm. Apatite is identified based on its calcium–phosphorus content. (For interpretation of the references to colour in this figure legend, the reader is referred to the web version of this article.)

that the pellet interior is composed of granular apatite interspersed with oval-shaped pores, reflecting internal heterogeneity and early post-depositional mineral enrichment.

Fig. 7E–F (also from YC4–110) depict an elongated fecal pellet with a distinct linear distribution of pore-filling minerals. In Fig. 7F, the internal ultrastructure is dominated by columnar apatite crystals aligned along the long axis of the pellet. This strongly directional fabric likely results from compaction and recrystallization during burial, with the residual pore network remaining within the apatite-rich matrix.

Fig. 8 presents SEM–EDS analyses of fecal pellets in the W–L shales, highlighting their role as sites of early diagenetic apatite mineralization. Fig. 8A shows an elongated fecal pellet embedded in the shale matrix and oriented parallel to bedding, indicative of low-energy depositional settings. Elemental mapping in Fig. 8B and C reveals weak calcium (Ca) signal and strong phosphorus (P) signal within the pellet. Fig. 8D–F provide the SEM image of an elliptic fecal pellet and the corresponding elemental distribution of calcium (Ca) and phosphorus (P). In Fig. 8E and F, bright granular phases of calcium (Ca) and phosphorus (P),

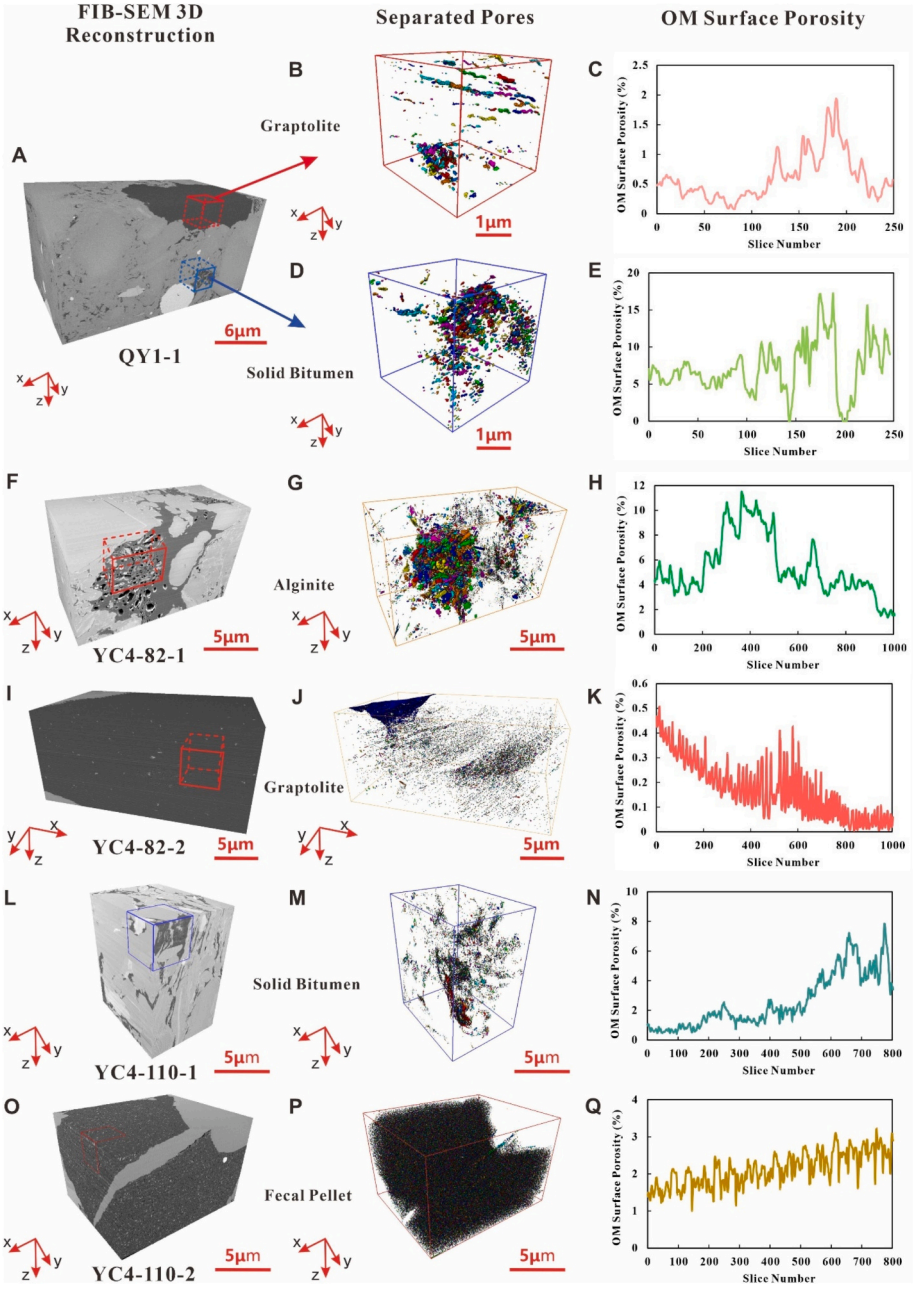

Fig. 9. Reconstructed 3D FIB-SEM volumes of different OM components in overmature W–L shales, illustrating pore network segmentation and slice-by-slice surface porosity profiles (right column). In the right column, the slice number zero corresponds to the origin of coordinates in the left and middle columns and represents the starting point for counts along the z-axis. In sample QY1–1, the 3D model (A) distinguishes graptolite (red box) and pyrobitumen (blue box), with segmented pore networks shown in (B) and (D), and their corresponding surface porosity profiles in (C) and (E). Alginite-rich OM from sample YC4–82-1 is visualized in (F-H), displaying a well-connected pore network (G) and surface porosity ranging from 4 % to 12 % with strong heterogeneity (H). Graptolite-dominated OM in sample YC4–82-2 (I-K) exhibits sparse, anisotropic pores (J) and very low porosity (<0.6 %) in (K). Pyrobitumen in sample YC4–110-1 (L–N) reveals vertically aligned, connected pores (M) with strong heterogeneity (N). Fecal pellet OM in sample YC4–110-2 (O–Q) features densely distributed nanoscale (P) and relatively stable porosity (4–6 %) across slices (Q). These visualizations highlight the strong influence of OM type on pore structure, connectivity, and porosity evolution in shale reservoirs. (For interpretation of the references to colour in this figure legend, the reader is referred to the web version of this article.)

confirming the presence of calcium phosphate minerals, primarily apatite.

Fig. 8G–I display higher magnification of the same pellet in Fig. 8D and exhibit a homogeneous internal texture and finely disseminated mineral phases. The EDS spectrum (Fig. 8H) highlights peaks for Ca, P, and F, consistent with fluorapatite, while the quantitative data (Fig. 8I) report Ca and P concentrations of 16.99 wt% and 5.71 wt%, respectively, along with 3.28 wt% F, indicating a well-crystallized phosphate phase. The elevated carbon (47.32 wt%) and oxygen (25.36 wt%) reflect the organic matrix and oxidized phases within the pellet.

Fig. 9 showcases a series of FIB-SEM 3D reconstructions and quantitative pore analyses of different macerals in overmature W–L shales, providing insights into pore morphology, connectivity (left and middle columns), and surface porosity distribution (right column) across maceral types. In particular, variations in OM surface porosity reflect the degree of homogeneity in the OM ultrastructure. Fig. 9A–E present sample QY1–1, highlighting a graptolite fragment (red cube) and adjacent pyrobitumen (blue cube). The segmented pore networks in Fig. 9B and D reveal sparse, isolated pores in graptolite, while pyrobitumen contains more complex, interconnected pore clusters. Corresponding surface porosity profiles (Fig. 9C and E) show that graptolite maintains low porosity (< 2.5 %) with minimal connectivity, whereas pyrobitumen reaches surface porosities up to ~18 %, reflecting enhanced storage capacity and strong heterogeneity. Fig. 9F–H illustrate alginite in sample YC4–82-1, showing a dense and continuous 3D pore network (Fig. 9G) and moderate to high porosity ranging from 4 % to 12 % with strong heterogeneity (Fig. 9H), consistent with preserved biological ultrastructures. Fig. 9I–K display another graptolite sample (YC4–82-2), while Fig. 9J showing a sparse and anisotropic pore distribution and a very low porosity profile (< 0.6 %, Fig. 9K), reaffirming its limited reservoir contribution. Fig. 9L–N focus on pyrobitumen in sample YC4–110-1, revealing vertically aligned, connected pores (Fig. 9M) and strong heterogeneity (Fig. 9N). Fig. 9O–Q depict a fecal pellet in sample YC4–110-2, featuring uniformly distributed nanopores (Fig. 9P) and consistent porosity values around 4–6 % across slices (Fig. 9Q), suggesting stable retention capacity.

3.4. Pore size distribution

Fig. 10 presents PSD data for key OM types, graptolite, alginite, pyrobitumen, and fecal pellets, derived from 3D FIB-SEM reconstructions. Pore size is defined as the radius of a sphere equivalent in volume to each segmented pore body. Fig. 10A–B illustrate the distribution of pores by count. Graptolite samples (QY1–1, YC4–82-2) exhibit narrow, unimodal distributions dominated by ultrafine pores (< 20 nm), with QY1–1 showing the lowest pore count, consistent with its low overall porosity (< 1 %). In contrast, pyrobitumen samples show broader PSDs, with a significant portion of pores between 40 and 100 nm, indicating enhanced storage potential. While graptolite-hosted pores are more numerous, Fig. 10B reveals that pyrobitumen-hosted pores are larger and more likely to contribute to effective porosity and fluid storage. Fig. 10C–D show pore distributions by volume. Alginite

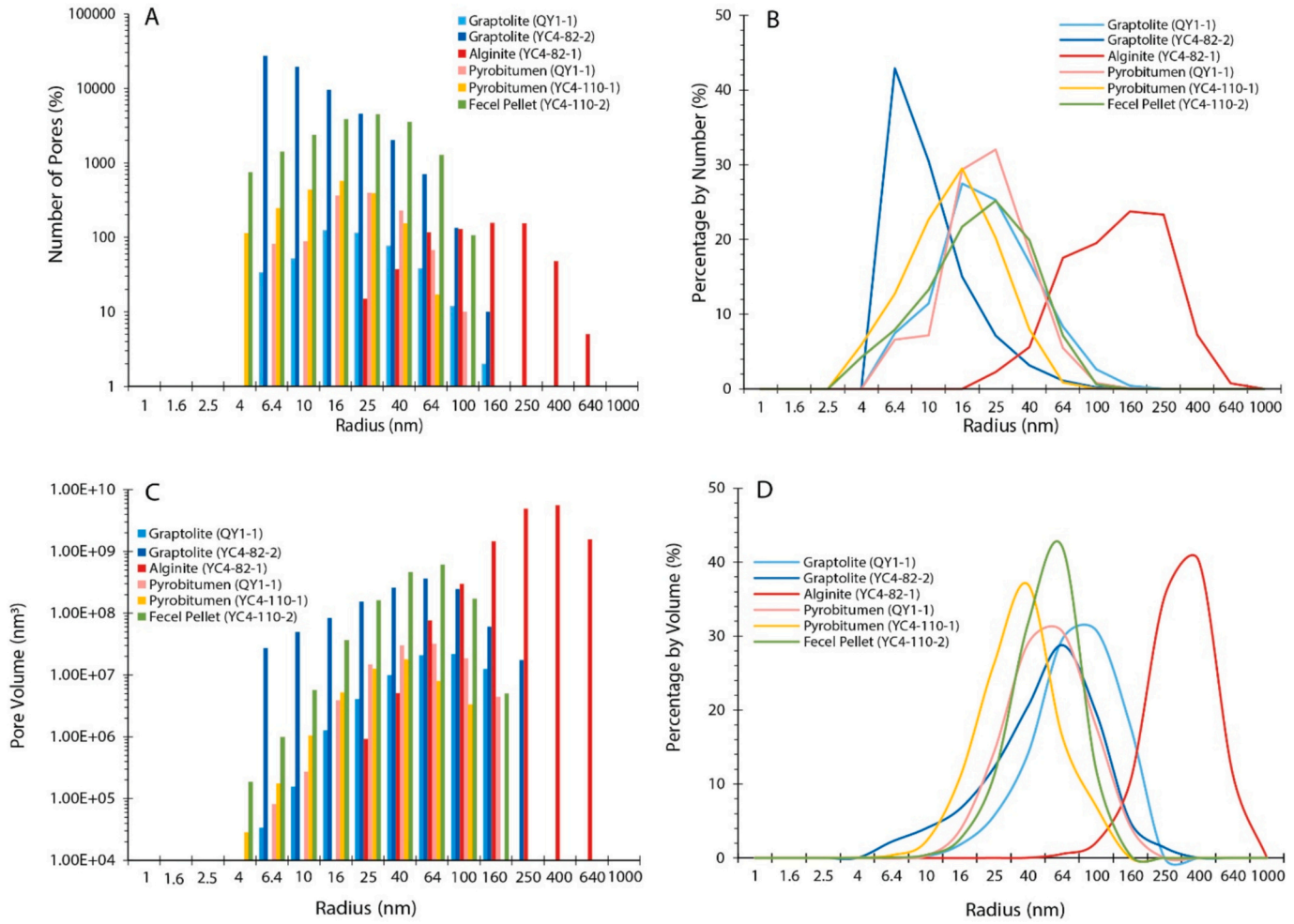

Fig. 10. Pore size distributions of alginite, pyrobitumen, graptolite, and fecal pellets, derived from 3D reconstructions of isolated pores shown in Fig. 9 (B, D, G, J, M, P). (A–B) Distribution by pore count; (C-D) Distribution by pore volume.

(YC4–82-1) displays the highest total pore volume, especially for pores >100 nm, underscoring its capacity for hydrocarbon storage. Pyrobitumen and fecal pellets exhibit moderate to broad volume distributions, with volume peaks typically between 40 and 100 nm pore sizes. Graptolite, although containing abundant small pores, contributes minimally to bulk pore volume due to its dominance of ultrafine structures. Fig. 10D confirms that pores >30 nm contribute the majority of total pore volume, consistent with prior findings (e.g., Ma et al., 2018) that pores in the 30–100 nm range have a better connectivity, while those >100 nm dominate effective storage. The presence of a broad PSD and non-monotonic decay in pyrobitumen (particularly YC4–82-1) also suggests microfracture development, consistent with previous interpretations (Ougier-Simonin et al., 2016).

3.5. *Permeability characterization in OM–hosted pore systems*

Fig. 11 and Table 3 present pore-scale permeability simulations for various OM types in the W–L shales, based on 3D FIB-SEM reconstructions and Navier–Stokes flow modeling. Permeability was calculated along the x, y, and z axes to evaluate anisotropy and fluid flow behavior across macerals. Graptolite in sample QY1–1 shows the lowest permeability (0.77, 1.87, 0.77 μD), with streamline visualizations (Fig. 11A–C) dominated by sparse blue paths, indicating poor connectivity and minimal fluid transport potential. In contrast, adjacent pyrobitumen from the same sample displays more isotropic permeability (0.77–0.78 μD), with streamlines (Fig. 11D–F) showing more continuous, green-to-red trajectories, suggesting better pore-throat development and possible microfracture presence.

Alginite in sample YC4–82-1 exhibits the highest and most isotropic permeability (9.42, 15.57, 10.55 μD), supported by dense, red-colored streamlines across all axes (Fig. 11G–I), reflecting a well-connected pore network. By contrast, graptolite in YC4–82-2 shows strong directional anisotropy, low permeability in the z direction (0.60 μD), but high permeability in x and y directions (9.42 and 15.57 μD) (Fig. 11J–L),

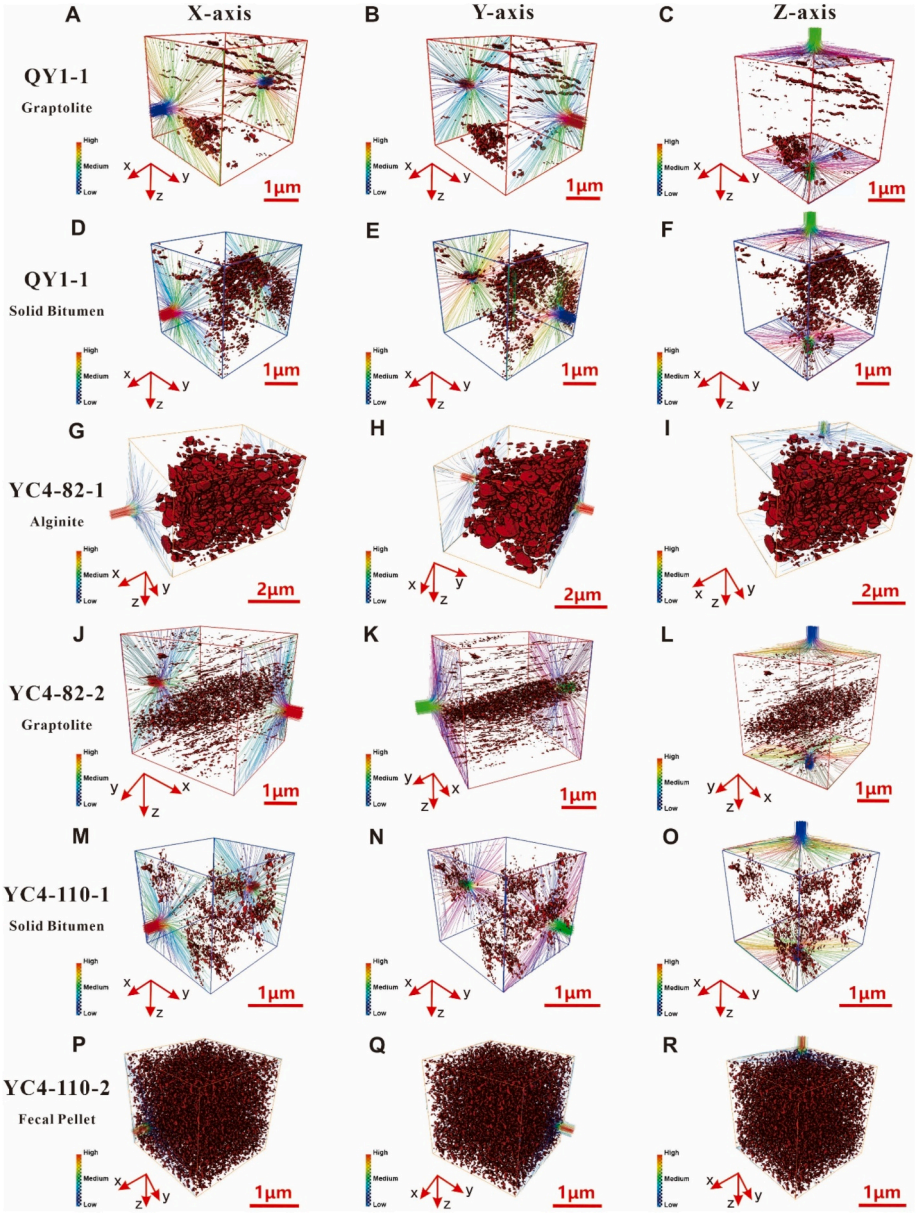

Fig. 11. Permeability simulation results for pyrobitumen, graptolite, and fecal pellets along three principal directions. Pore networks used in the simulations were extracted from the red-highlighted regions in Fig. 9. (For interpretation of the references to colour in this figure legend, the reader is referred to the web version of this article.)

Table 3
Absolute permeability tensors of pyrobitumen, graptolites, and fecal pellets calculated using the direct Navier–Stokes (N-S) algorithm in Avizo®. Corresponding visualizations are shown in Fig. 9. (Note: 1 μDarcy ≈ 10^{-18} m^2).

Sample ID	FIB-SEM 3D reconstruction physical dimensions (μm)	OM type	Calculated OM porosity (%)	3D reconstruction physical dimensions (μm)	Direction	K (μDarcy)
QY1–1	22 × 11.4 × 12.83	Graptolite	0.61	2.5 × 2.5 × 2.5	x	0.77
					y	1.87
					z	0.77
		Pyrobitumen	6.41	2.5 × 2.5 × 2.5	x	0.77
					y	0.74
					z	0.78
YC4–82-1	16.87 × 5.08 × 11.17	Alginite	13.07	5.82 × 3.57 × 6.94	x	9.42
					y	15.57
					z	10.55
YC4–82-2	24.79 × 15.37 × 11.75	Graptolite	0.61	4 × 4 × 4	x	9.42
					y	15.57
					z	0.60
YC4–110-1	5.79 × 7.62 × 9.38	Pyrobitumen	1.98	2.5 × 2.5 × 2.5	x	0.74
					y	0.74
					z	0.74
YC4–110-2	14.57 × 6.74 × 9.38	Fecal Pellet	4.90	2.5 × 2.5 × 2.5	x	0.81
					y	0.77
					z	0.77

consistent with laminar structural alignment enhancing flow directionally.

Pyrobitumen in YC4–110-1 shows relatively uniform permeability (~0.74 μD) in all directions (Fig. 11M–O), with slightly improved connectivity compared to QY1–1, reflecting heterogeneity in pyrobitumen-hosted pore systems. Finally, fecal pellets in YC4–110-2 yield intermediate but isotropic permeability (0.77–0.81 μD), with densely packed, evenly distributed streamline patterns across axes (Fig. 11P–R).

4. Discussion

4.1. Coupled effects of volcanism, biogenic input, and diagenesis on organic enrichment and pore system evolution

Volcanism exerted a fundamental dual control on the development of organic-rich shale and pore system evolution in the Wufeng–Longmaxi (W–L) formations of the Upper Yangtze region. Wu et al. (2018) distinguished two major transgressive systems tracts (TSTs): TST1 in the Upper Ordovician Wufeng Formation and TST2 in the Lower Silurian Longmaxi Formation. TST1 is characterized by dense bentonite deposition (frequency > 1.5 layers/Ma; cumulative thickness ratio > 1 %), while TST2 exhibits much sparser volcanic input. Intense volcanism during TST1 supplied large volumes of nutrient-rich ash (containing N, P, Si, Fe, and Al), which stimulated phytoplankton proliferation and enhanced primary productivity, consequently favoring the widespread development of euxinic conditions and high organic matter preservation (Zhang et al., 2020; Qiu et al., 2022; Grasby et al., 2024). This combination of volcanic fertilization and persistent anoxia resulted in the accumulation of black, siliceous shales with higher TOC content compared to the relatively leaner, less anoxic shales of TST2. However, recent cyclostratigraphic and geochemical studies have revealed that sedimentation during the Longmaxi transgression was not entirely continuous; multiple cryptic hiatuses interrupt the fine-grained succession, reflecting subtle but significant depositional discontinuities. Liu et al. (2025) identified six such hiatuses (H1–H6) within the Lower Silurian Longmaxi Formation using an integrated sedimentological, geochemical, and Evolutive Spectral Analysis (ESA) approach, demonstrating that many of these surfaces correspond to relative sea-level falls driven by glacio-eustasy and tectonism associated with the Kwangsian Orogeny. These episodic interruptions—linked to bottom-current erosion, oxidation, and non-depositional intervals—likely modulated organic accumulation and diagenetic processes, influencing the spatial variability of TOC enrichment and pore system heterogeneity across the basin. Therefore, the interplay between volcanic nutrient supply, sea-level–controlled sedimentary hiatuses, and anoxia collectively governed both the stratigraphic architecture and the geochemical evolution of the W–L shale system in the Upper Yangtze region.

Despite uniformly high thermal maturity (EqVRo 3.89–4.20 %), TOC variability reflects differences in primary input, preservation efficiency, and diagenetic pathways, rather than maturity alone. This highlights the critical roles of depositional redox conditions in OM preservation and origin in controlling maceral assemblages and associated pore evolution in overmature marine shales.

The depositional model (Fig. 12A) illustrates that volcanic ash influx stimulated diverse biogenic inputs, including phytoplankton, algae, radiolarians, and fecal pellets (Gonzalez and Smetacek, 1994; Simon et al., 2002; Grossart et al., 2006). Aggregated, fast-sinking fecal pellets facilitated rapid burial (Martin et al., 1987; Poulsen and Iversen, 2008; Manno et al., 2015; Steinberg and Landry, 2017), while microbial restructuring and early phosphatization stabilized OM particles (Hirschler et al., 1990; Benitez-Nelson, 2000; MacIver et al., 2021). This led to the formation of phosphatized fecal pellets with well-preserved nanoporous ultrastructures (Kondla et al., 2016). The coexistence of alginite, pyrobitumen, graptolites, and fecal pellets reflects variable productivity, sedimentation rates, and redox stratification during deposition (Lampitt et al., 1990; Lalande et al., 2011; Guo and Zhang, 2014; Dagg et al., 2014; Turner, 2015; Ma et al., 2016; Cao et al., 2020).

Maceral identification in such overmature settings is complex and requires careful evaluation. Reflectance-based evidence supports that all hydrogen-rich liptinite macerals, including alginite, have been thermally transformed into pyrobitumen (Mastalerz et al., 2018; Wei et al., 2021; Teng et al., 2022; Huang et al., 2025). Although some preserved features (e.g., Fig. 4A–D) suggest cellular morphologies, we conservatively interpret them as alginite-derived pyrobitumen. No intact algal palynomorphs (e.g., Volvox-type) or lamalginite have been observed under transmitted light or SEM, consistent with full bituminization (Pang et al., 2018; Cao et al., 2021; Wang et al., 2022). Thus, macroporous textures are attributed to in situ thermal degradation of original algal OM.

Graptolites are common in our samples and show reflectance anisotropy and laminated cortical structures under plane-polarized (PPL) and cross-polarized (XPL). According to Hartkopf-Fröder et al. (2015) and Hoffknecht (1991), graptolites are composed of fusellar and cortical tissues within a tubarium. Our FIB-SEM observations reveal aligned nanoporosity within non-granular graptolites, but these pores are poorly interconnected and display pronounced anisotropy.

Fig. 12B summarizes maceral-specific diagenetic pathways. Pyrobitumen forms shrinkage and crack-related nanopores through in situ

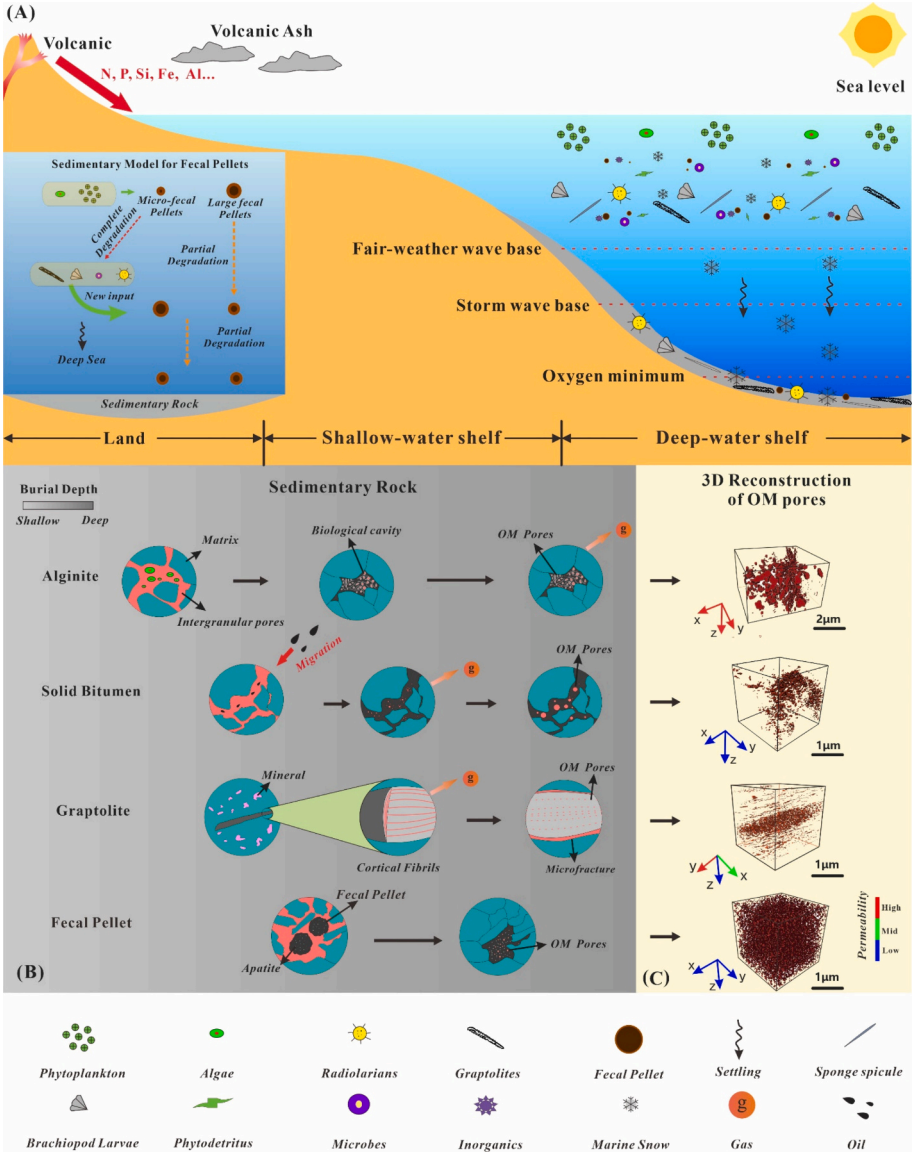

Fig. 12. Schematic diagram illustrating the evolutionary stages of OM-hosted pore systems in pyrobitumen, graptolites, and fecal pellets, from initial sedimentation through diagenesis in a marine depositional setting. (A) was modified from Turner (2015) and Tang et al. (2020).

degradation of precursor alginite. In fecal pellets, early microbial alteration and apatite precipitation preserve isotropic nano-porous textures. Graptolites show layered, anisotropic porosity aligned along cortical laminations. These patterns are quantitatively supported by 3D FIB-SEM data (Fig. 12C): pyrobitumen shows porosity up to 10 % with moderate anisotropy; fecal pellets ~5 % porosity with isotropic connectivity; graptolites <1 % porosity; and alginite-derived pyrobitumen exhibits the most favorable macropore development (Ko et al., 2016; İnan et al., 2018).

Overall, OM-hosted pore development in W–L shales is governed primarily by maceral type, redox environment, and early diagenetic stabilization, not maturity alone (Gowing and Silver, 1985; Turner, 2002; MacIver et al., 2021). Volcanic nutrient influx, microbial phosphatization, and ultrastructure preservation collectively facilitated an efficient framework for nanopore generation. The distinct pore architectures—especially in pyrobitumen and phosphatized fecal pellets, provide key insights for sweet spot prediction in overmature shale gas systems.

4.2. Maceral-specific pore architecture and diagenetic stabilization in overmature W–L shales

In the overmature W–L shales (EqVR ≈ 4.0 %), OM-hosted pore systems have been observed to differ significantly across maceral types, with variations in porosity, permeability, morphology, and diagenetic preservation. These differences are governed not by maturity alone, but by the biological origin of the macerals and their associated diagenetic stabilization processes (Wang et al., 2020; Lyu et al., 2022).

Pyrobitumen, the most abundant organic component in the studied samples, has been identified as exhibiting irregular outlines and equant pore structures, morphologically resembling Type I pyrobitumen as described by Wei et al. (2021). Although no formal classification has been applied, the pyrobitumen observed in this study also aligns with the migrated pyrobitumen category proposed by Wang et al. (2023), particularly in its quartz- and pyrite-hosted occurrences. Internal pores within pyrobitumen, ranging from 20 to over 100 nm, have been shown to develop through thermal shrinkage during bituminization and are stabilized by diagenetic mineral infilling such as framboidal pyrite and authigenic illite (Zargari et al., 2015; Gao et al., 2020). These pores

exhibit moderate connectivity and an estimated permeability of ~0.74–0.78 μD, with porosity ranging from 4 % to 12 % (Fig. 9D–F; Table 3). Preservation of these pore systems under deep burial conditions is attributed to the interaction of OM with surrounding minerals (Ougier-Simonin et al., 2016; Mastalerz et al., 2018).

Some pyrobitumen domains display large, spherical, or sponge-like pore networks with macropores exceeding 200 nm, especially in quartz-hosted zones, which are morphologically and texturally consistent with those derived from alginite (Xie and Hao, 2022). These features are cautiously referred to as alginite-derived pyrobitumen, following recommendations by Mastalerz et al. (2018), given the absence of definitive palynological or biomarker evidence. The possibility of a precursor alginite origin is supported by their high porosity and improved connectivity, although transformation into pyrobitumen at high thermal maturity complicates definitive identification (Wei et al., 2021; Teng et al., 2022).

Alginite, when preserved, exhibits its characteristic cellular ultrastructure and develops extensive intercellular pore systems during maturation. These pore systems include isotropic macropores (> 50 nm) that are well connected and exhibit high porosity (up to 13 %) and permeability values exceeding 15 μD (Figs. 4B–D; 9F-H), surpassing those of other OM types (Ma et al., 2018; Wang and Jin, 2019; MacIver et al., 2021). The retention of this pore architecture appears to be intrinsic, requiring no mineral support to resist compaction. While alginite remains challenging to identify in overmature shales, morphological similarities to benthic alginite (Alginite I), characterized by lattice-like laminae and sponge-like pores, have been noted (Hu et al., 2020; Pang et al., 2021). Nonetheless, given the ambiguity, such domains must be interpreted with caution and integrated with additional optical and geochemical data.

Phosphatized fecal pellets constitute a distinct maceral type, distinguished by dense nanoporous structures (40–160 nm) within Ca- and P-enriched matrices, as confirmed by EDS mapping (Fig. 8B, E). These features result from early diagenetic phosphatization, whereby apatite and fluorapatite precipitate during microbial decomposition, forming mechanically stable frameworks (Hirschler et al., 1990; Benitez-Nelson, 2000; MacIver et al., 2021). This mineral reinforcement effectively resists compaction and preserves porosity (~5 %) and isotropic permeability (~0.77–0.81 μD), even under deep burial conditions (Fig. 11P–R; Table 3). Though relatively rare, these fecal pellets contribute significantly to storage and flow due to their compact-resistant pore networks.

Graptolites, though abundant and of great stratigraphic and thermal significance, exhibit extremely limited reservoir potential due to their inherently low porosity and permeability. Their cortical and fusellar tissues typically host narrow, annular pores aligned along the rhabdosome axis (Teichmüller, 1978; Bubeck et al., 2017; Shi et al., 2020), yet these pores are generally <20 nm and display very poor connectivity (Fig. 6). FIB-SEM and flow simulation analyses confirm their exceptionally low porosity (< 0.6 %) and permeability (< 0.35 μD), with modeled values in some cases below 0.1 μD (Xu et al., 2020). Recent high-resolution AFM observations from the Baltic Basin further demonstrate that graptolite periderm nanoporosity remains extremely low (0.16–0.28 %) even at maturities near the oil-to-gas window, with only limited development of secondary micropores <5 nm associated with structural degradation during advanced thermal evolution (Morga and Wrzalik, 2025). These findings indicate that graptolite-hosted pore systems contribute negligibly to hydrocarbon storage or flow, although granular fabrics may become slightly more generative than non-granular ones at higher maturities. In contrast, the optical and petrological properties of graptolites make them highly valuable for thermal maturity evaluation in vitrinite-absent marine shales. Graptolites in the Ordovician–Silurian Wufeng–Longmaxi and analogous formations display distinct biaxial optical behavior, with reflectance varying systematically between sections parallel and perpendicular to bedding (Wu et al., 2025). Such anisotropy reflects increasing bireflectance and structural ordering during maturation, and newly established empirical equations now permit reliable conversion between reflectance values obtained from different orientations. Thus, while graptolites are ineffective as reservoir media, their well-preserved ultrastructure and anisotropic reflectance characteristics render them critical organic indicators for reconstructing the thermal and diagenetic evolution of Lower Paleozoic marine shales (Hartkopf-Fröder et al., 2015; Wang et al., 2025).

Across all maceral types, the role of diagenetic mineralization in stabilizing OM-hosted pore systems is significant. Phosphatization has been shown to be critical in preserving nanopores in fecal pellets, while mineral infilling in pyrobitumen enhances pore integrity under compaction (Minisini et al., 2025). Graptolites, in contrast, lack effective mineral support and undergo tissue degradation with thermal stress. The potential influence of post-maturation uplift on microcrack development, especially in brittle OM domains, has been acknowledged; however, pore architectures documented here remain consistent with those in unexhumed shale analogs (Sun et al., 2024; Teng et al., 2022). Moreover, all flow simulations were conducted under pressure and temperature conditions replicating in situ peak gas generation phases.

In summary, OM-hosted pore networks in the W–L shales display a clear maceral-specific hierarchy in both storage and transport performance—alginite > pyrobitumen ≈ fecal pellets > > graptolites—driven by biological origin, pore geometry, and mineral stabilization (Fig. 11; Table 3). These findings are consistent with global analogues such as the Barnett (Slatt and O'Brien, 2011) and Eagle Ford (Reed et al., 2020), as well as with prior studies on the Longmaxi shales (Wei et al., 2021). Accurate maceral identification, including discrimination between pyrobitumen and altered alginite, is essential for interpreting FIB-SEM data and reconstructing reservoir quality in overmature shale systems. Future work should integrate reflectance measurements (e.g., graptolite reflectance, bitumen reflectance), morphological imaging, and mineralogical analyses to refine understanding of OM pore evolution and gas storage potential in these deep, thermally mature marine shale reservoirs (Curtis et al., 2012; Waliczek et al., 2019; Wang et al., 2020; Klaver et al., 2024; Wang et al., 2025).

4.3. Controls on gas storage and deliverability

The gas storage and production potential of the W–L shales is fundamentally governed by the type, abundance, diversity, and preservation state of OM-hosted pore systems, which collectively determine both the volumetric storage capacity and the efficiency of hydrocarbon flow and extraction. Although all analyzed samples are uniformly overmature (EqVR ~4.0 %; Table 1), FIB-SEM imaging and numerical simulations reveal significant differences in nanoscale pore structure and permeability across maceral types (Wei et al., 2021; Wang et al., 2023).

Among the various OM components, alginite shows the most favorable pore architecture for gas storage and flow. In high-TOC samples like YC4–110, preserved algal cell walls form interconnected macropores (>100 nm), resulting in high porosity (>10 %) and the highest permeability (~15.6 μD) observed (Figs. 9F–H; 12C; Table 3). These cellular macropores provide large free gas storage volumes and enable rapid gas transport, making alginite-rich zones prime targets for shale gas development (Ma et al., 2018; Reed et al., 2020; Liu et al., 2022). However, due to thermal alteration at EqVR >2.6 %, alginite preservation is rare, and some structures interpreted as alginite (e.g., Xie and Hao, 2022) may be vesicular pyrobitumen, necessitating stricter maceral classification (Landis and Castaño, 1995; Mastalerz et al., 2018).

Pyrobitumen, the most abundant maceral in the W–L shales, contributes a bimodal pore system (10–50 nm), combining both mesopores and micropores generated through thermal shrinkage, oil cracking, and secondary gas generation (Ko et al., 2016; İnan et al., 2018). These pores accommodate free gas within larger voids, while smaller micropores provide abundant surface area for adsorbed gas storage. Despite greater heterogeneity and somewhat lower permeability (~ 0.75 μD) than

alginite, pyrobitumen-hosted pores represent an important component of the reservoir's pore network, particularly in thermally mature sections where oil has been fully cracked to gas (Curtis et al., 2012; Mastalerz et al., 2018). FIB-SEM observations (Fig. 5) show vesicular and irregular voids ranging from tens to hundreds of nanometers. Permeability values derived from simulations range from 0.74 to 0.78 μD (Fig. 9D–F; Table 3). Despite slightly lower permeability than alginite, pyrobitumen-hosted porosity remains a major contributor to gas storage due to its widespread distribution and partially connected pore networks (Ko et al., 2016; Wang et al., 2023).

Phosphatized fecal pellets, stabilized by early apatite mineralization, serve as an additional nano-porous domain that favors adsorbed gas retention. Their compact, isotropic architecture, characterized by pores ranging from 40 to 160 nm, remains mechanically stable under deep burial, consistently maintaining moderate porosity (~ 5 %) and permeability (~ 0.8 μD, Fig. 11P–R; Table 3) (Hirschler et al., 1990; Krajewski, 2013; Steinberg and Landry, 2017; MacIver et al., 2021).

By contrast, graptolite-hosted pores are structurally constrained, aligned along cortical lamellae, and poorly connected. These annular or linear nanopores are mostly <20 nm in diameter (Fig. 6), with extremely low porosity (<0.6 %) and permeability <0.35 μD, making graptolites ineffective for gas storage or flow (Bubeck et al., 2017; Shi et al., 2020; Xu et al., 2020). However, their ultrastructure and optical reflectance properties remain valuable for assessing thermal maturity (Hartkopf-Fröder et al., 2015; Wang et al., 2020).

Flow simulations and 3D FIB-SEM reconstructions establish a consistent hierarchy of OM-hosted permeability (Figs. 10–11), aligning well with broader pore classification frameworks proposed in previous shale gas studies (Lampitt et al., 1990; Slatt and O'Brien, 2011; Wang and Jin, 2019). Beyond OM type alone, depositional conditions including water column stratification, nutrient enrichment, and microbial restructuring played crucial roles in OM preservation and pore system development (Martin et al., 1987; Simon et al., 2002; Lalande et al., 2011; Dagg et al., 2014; Manno et al., 2015; Li et al., 2021).

In synthesis, based on the integration of new data with earlier findings (Guo and Zhang, 2014; Zhang et al., 2020; Teng et al., 2022), it is concluded that effective shale gas storage capacity in the W–L system is critically dependent on the preservation of compact OM-hosted nanoporosity. The primary storage framework is provided by alginite and pyrobitumen, while durable, stable secondary capacity is offered by fecal pellets. A refined basis for targeted reservoir characterization, sweet spot identification, and production optimization in overmature marine shale systems is thereby established.

5. Conclusion

This study systematically demonstrates that the pore architecture, gas storage, and flow potential of the overmature W–L shales are fundamentally controlled by OM type, depositional conditions, and diagenetic stabilization rather than maturity or TOC content alone. Although all samples exhibit consistently high thermal maturity (EqVRo 3.89–4.20 %), TOC content varies widely (0.47–5.48 wt%), reflecting variations in primary productivity, organic input, and preservation during deposition. Volcanogenic nutrient enrichment, strong water column stratification, and rapid burial of fecal aggregates facilitated OM accumulation, microbial restructuring, and early diagenetic mineralization.

Quantitative SEM and FIB-SEM analyses reveal distinct pore systems among macerals. Alginite preserves biogenic cellular ultrastructures, forming highly connected macro-porous networks (>100 nm) with the highest porosity (> 10 %) and permeability (~ 15.6 μD), making it the most favorable OM for gas storage and deliverability. Pyrobitumen, derived from alginite transformation, develops shrinkage-induced meso- and micropores during oil cracking, contributing significant porosity (4–13 %) and moderate permeability (~ 0.75 μD), with framboidal pyrite providing additional mechanical stabilization. Fecal pellets, stabilized by early apatite mineralization, exhibit dense, isotropic nanopores (40–160 nm), consistently maintaining ~5 % porosity and permeability (~ 0.8 μD). In contrast, graptolites contribute limited storage due to poorly connected, elongated cortical pores (< 20 nm) with porosity <0.6 % and very low permeability (< 0.35 μD).

Pore size distribution and permeability simulations establish a hierarchical ranking: alginite > pyrobitumen ≈ fecal pellets > > graptolites. This hierarchy highlights the critical role of OM-specific ultrastructures and diagenetic mineralization in preserving nanoporosity and sustaining flow capacity through burial compaction. The strong coupling of biological origin, microbial modification, and early mineral infill underscores that effective pore preservation is not solely a function of maturity but results from the integrated depositional-diagenetic evolution of OM.

These findings provide a refined framework for evaluating overmature marine shale systems, where detailed OM type analysis and 3D pore characterization are essential for accurately predicting storage capacity, flow behavior, and sweet spot distribution. The integrated approach outlined here offers direct implications for reservoir quality assessment, production optimization, and resource development strategies in complex shale gas plays.

CRediT authorship contribution statement

Yong Ma: Writing – review & editing, Writing – original draft, Validation, Methodology, Conceptualization. **Omid H. Ardakani:** Writing – review & editing, Writing – original draft, Methodology, Conceptualization. **Dahua Li:** Writing – review & editing, Resources, Data curation. **Jianbin Ma:** Writing – review & editing, Investigation, Data curation. **Ningning Zhong:** Writing – review & editing, Supervision, Conceptualization. **Haiping Huang:** Writing – review & editing, Writing – original draft, Conceptualization.

Declaration of competing interest

The authors declare no competing interests.

Acknowledgements

This work was supported by the National Natural Science Foundation of China (Grant No. 42173030, 42473034, and 42572157), the Open Project from the Key Laboratory of Shale Gas Exploration, Ministry of Natural Resources (KLSGE-202406) and National Science and Technology Major Project (2025ZD1400400). Prof. Steve Larter from the University of Calgary and two reviewers are gratefully acknowledged for their constructive comments, which significantly enhanced the quality of this manuscript.

Data availability

Data will be made available on request.

References

Ardakani, O.H., Sanei, H., Ghanizadeh, A., Lavoie, D., Chen, Z., Clarkson, C.R., 2018. Do all fractions of organic matter contribute equally in shale porosity? A case study from Upper Ordovician Utica Shale, southern Quebec, Canada. Mar. Pet. Geol. 92, 794–808.

Benitez-Nelson, C.R., 2000. The biogeochemical cycling of phosphorus in marine systems. Earth-Sci. Rev. 51, 109–135.

Bubeck, A., Walker, R.J., Healy, D., Dobbs, M., Holwell, D.A., 2017. Pore geometry as a control on rock strength. Earth Planet. Sci. Lett. 457, 38–48.

Callow, B., Falcon-Suarez, I., Ahmed, S., Matter, J., 2018. Assessing the carbon sequestration potential of basalt using X–ray micro–CT and rock mechanics. Int. J. Greenhouse Gas Control 70, 146–156.

Callow, B., Falcon-Suarez, I., Marin-Moreno, H., Bull, J.M., Ahmed, S., 2020. Optimal X–ray micro–CT image based methods for porosity and permeability quantification in heterogeneous sandstones. Geophys. J. Int. 223, 1210–1229.

Cao, T., Xu, H., Liu, G., Deng, M., Cao, Q., Yu, Y., 2020. Factors influencing microstructure and porosity in shales of the Wufeng–Longmaxi formations in northwestern Guizhou, China. J. Pet. Sci. Eng. 191, 107181.
Cao, Q., Jiang, K., Wen, Z., Wang, X., Qi, M., Yin, Z., 2021. Characteristics of organic matter pores and the relationship with current pressure system of lower Silurian Longmaxi Shales in Dingshan Field, Southern Sichuan, China. Geofluids 2021, 9967479.
Curtis, M.E., Cardott, B.J., Sondergeld, C.H., Rai, C.S., 2012. Development of organic porosity in the Woodford Shale with increasing thermal maturity. Int. J. Coal Geol. 103, 26–31.
Dagg, M.J., Jackson, G.A., Checkley Jr., D.M., 2014. The distribution and vertical flux of fecal pellets from large zooplankton in Monterey bay and coastal California. Deep Sea Res. Part I 94, 72–86.
Gao, Z., Fan, Y., Xuan, Q., Zheng, G., 2020. A review of shale pore structure evolution characteristics with increasing thermal maturities. Adv. Geo-Energy Res. 4, 247–259.
Garum, M., Glover, P.W., Lorinczi, P., Drummond-Brydson, R., Hassanpour, A., 2020. Micro–and nano–scale pore structure in gas shale using Xμ–CT and FIB–SEM techniques. Energy Fuel 34, 12340–12353.
Gonzalez, H.E., Smetacek, V., 1994. The possible role of the cyclopoid copepod *Oithona* in retarding vertical flux of zooplankton faecal material. Mar. Ecol. Prog. Ser. 113, 233–246.
Gowing, M.M., Silver, M.W., 1985. Minipellets: a new and abundant size class of marine fecal pellets. J. Mar. Res. 43, 395–418.
Grasby, S.E., Ardakani, O.H., Liu, X., Bond, D.P., Wignall, P.B., Strachan, L.J., 2024. Marine snowstorm during the Permian–Triassic mass extinction. Geology 52, 120–124.
Grossart, H.P., Kiørboe, T., Tang, K.W., Allgaier, M., Yam, E.M., Ploug, H., 2006. Interactions between marine snow and heterotrophic bacteria: aggregate formation and microbial dynamics. Aquat. Microb. Ecol. 42, 19–26.
Guo, T., Zhang, H., 2014. Formation and enrichment mode of Jiaoshiba shale gas field, Sichuan Basin. Pet. Explor. Dev. 41, 31–40.
Hackley, P.C., Cardott, B.J., 2016. Application of organic petrography in north American shale petroleum systems: a review. Int. J. Coal Geol. 163, 8–51.
Hartkopf-Fröder, C., Königshof, P., Littke, R., Schwarzbauer, J., 2015. Optical thermal maturity parameters and organic geochemical alteration at low grade diagenesis to anchimetamorphism: a review. Int. J. Coal Geol. 150–151, 74–119.
Hirschler, A., Lucas, J., Hubert, J.C., 1990. Apatite genesis: a biologically induced or biologically controlled mineral formation process? Geomicrobiol J. 8, 47–56.
Hoffknecht, A., 1991. Mikropetrographische, organisch-geochemische, mikrothermometrische und mineralogische Untersuchungen zur Bestimmung der organischen Reife von Graptolithen-Periderm. Gött. Arb. Geol. Paläontol. 48, 1–98.
Hu, G., Pang, Q., Jiao, K., Hu, C., Liao, Z., 2020. Development of organic pores in the Longmaxi Formation overmature shales: combined effects of thermal maturity and organic matter composition. Mar. Pet. Geol. 116, 104314.
Huang, H., Zhang, H., Ma, Z., Yang, X., Ma, Y., Zheng, L., 2025. Evolution of pore structure in the Upper cretaceous Second White Speckled Shale during thermal maturation: insights from artificial and naturally matured samples. Int. J. Coal Geol. 302, 104728.
İnan, S., Al Badairy, H., İnan, T., Al Zahrani, A., 2018. Formation and occurrence of organic matter–hosted porosity in shales. Int. J. Coal Geol. 199, 39–51.
Katz, B.J., Arango, I., 2018. Organic porosity: a geochemist's view of the current state of understanding. Org. Geochem. 123, 1–16.
Klaver, J., Grohmann, S., Gaus, G., Abu-Mahfouz, I.S., Patzek, T., Vahrenkamp, V., Urai, J.L., 2024. Microstructural BiB-SEM investigation of Upper cretaceous Jordanian carbonate-rich oil shales bearing type II-S kerogen. Int. J. Earth Sci. 113, 2233–2249.
Knapp, L.J., Ardakani, O.H., Uchida, S., Nanjo, T., Otomo, C., Hattori, T., 2020. The influence of rigid matrix minerals on organic porosity and pore size in shale reservoirs: Upper Devonian Duvernay Formation, Alberta, Canada. Int. J. Coal Geol. 227, 103525.
Ko, L.T., Loucks, R.G., Zhang, T., Ruppel, S.C., Shao, D., 2016. Pore and pore network evolution of Upper cretaceous Boquillas (Eagle Ford–equivalent) mudrocks: results from gold tube pyrolysis experiments. Am. Assoc. Pet. Geol. Bull. 100, 1693–1722.
Kondla, D., Sanei, H., Clarkson, C.R., Ardakani, O.H., Wang, X., Jiang, C., 2016. Effects of organic and mineral matter on reservoir quality in a Middle Triassic mudstone in the Canadian Arctic. Int. J. Coal Geol. 153, 112–126.
Krajewski, K.P., 2013. Organic matter–apatite–pyrite relationships in the Botneheia Formation (Middle Triassic) of eastern Svalbard: Relevance to the formation of petroleum source rocks in the NW Barents Sea shelf. Mar. Pet. Geol. 45, 69–105.
Lalande, C., Bauerfeind, E., Nöthig, E.M., 2011. Downward particulate organic carbon export at high temporal resolution in the eastern Fram Strait: influence of Atlantic Water on flux composition. Mar. Ecol. Prog. Ser. 440, 127–136.
Lampitt, R.S., Noji, T., Von Bodungen, B., 1990. What happens to zooplankton faecal pellets? Implications for material flux. Mar. Biol. 104, 15–23.
Landis, C.R., Castaño, J.R., 1995. Maturation and bulk chemical properties of a suite of solid hydrocarbons. Org. Geochem. 22, 137–149.
Li, K., Ren, Y., Ke, Z., Li, G., Tan, Y., 2021. Vertical distributions of epipelagic and mesopelagic zooplankton in the continental slope of the northeastern South China Sea. J. Trop. Oceanogr. 40, 61–73 (in Chinese with English abstract).
Lis, G.P., Topór, T., Mastalerz, M., 2025. Organic matter content and its role in shale porosity development with maturity: Insights from Baltic Basin Silurian shales. Int. J. Coal Geol. 301, 104713.
Liu, S., Yang, Y., Deng, B., Zhong, Y., Wen, L., Sun, W., et al., 2021. Tectonic evolution of the Sichuan Basin, Southwest China. Earth-Sci. Rev. 213, 103470.
Liu, B., Mastalerz, M., Schieber, J., 2022. SEM petrography of dispersed organic matter in black shales: a review. Earth-Sci. Rev. 224, 103874.
Liu, Y., Xian, B., Wu, Q., Lu, Z., Shi, H., Wu, M., et al., 2025. Unraveling hiatuses in black shale: mechanisms and implications from the lower Silurian Longmaxi formation, South China. Int. J. Coal Geol. 310, 104869.
Löhr, S.C., Baruch, E.T., Hall, P.A., Kennedy, M.J., 2015. Is organic pore development in gas shales influenced by the primary porosity and structure of thermally immature organic matter? Org. Geochem. 87, 119–132.
Loucks, R.G., Reed, R.M., 2014. Scanning–electron–microscope petrographic evidence for distinguishing organic–matter pores associated with depositional organic matter versus migrated organic matter in mudrocks. GCAGS J. 3, 51–60.
Loucks, R.G., Reed, R.M., Ruppel, S.C., Jarvie, D.M., 2009. Morphology, genesis, and distribution of nanometer–scale pores in siliceous mudstones of the Mississippian Barnett Shale. J. Sediment. Res. 79, 848–861.
Loucks, R.G., Reed, R.M., Ruppel, S.C., Hammes, U., 2012. Spectrum of pore types and networks in mudrocks and a descriptive classification for matrix–related mudrock pores. Am. Assoc. Pet. Geol. Bull. 96, 1071–1098.
Luo, Q.Y., Zhong, N.N., Zhang, Y., Dai, Na, Zhang, W., 2016. Graptolite-derived organic matter in the Wufeng-Longmaxi formations (upper Ordovician-lower Silurian) of southeastern Chongqing, China: implications for gas shale evaluation. Int. J. Coal Geol. 153, 87–98.
Lyu, P., Meng, J., Pan, R., Yi, X., Yue, T., Zhang, N., 2022. Characteristics and differences analysis for thermal evolution of Wufeng–Longmaxi Shale, Southern Sichuan Basin, SW China. Minerals 12, 906.
Ma, Y., Zhong, N., Cheng, L., Pan, Z., Dai, N., Zhang, Y., Yang, L., 2016. Pore structure of the graptolite–derived OM in the Longmaxi Shale, southeastern Upper Yangtze Region, China. Mar. Pet. Geol. 72, 1–11.
Ma, L., Slater, T., Dowey, P.J., Yue, S., Rutter, E.H., Taylor, K.G., Lee, P.D., 2018. Hierarchical integration of porosity in shales. Sci. Rep. 8, 11683.
Ma, Y., Xin, Z., Song, J., Li, D., Zhu, D., Zhang, H., Zhong, N., 2025a. Geological controls on shale gas accumulation in a synclinal reservoir and implications for natural gas migration. Mar. Pet. Geol. 178, 107404.
Ma, Y., Hu, H., Pan, Z., Zhong, N., Jiang, F., Yang, C., et al., 2025b. Matrix permeability anisotropy of organic–rich marine shales and its geological implications: Experimental measurements and microscopic analyses. Int. J. Coal Geol. 297, 104670.
MacIver, M.R., Sablok, A., Pawlik, M., 2021. Apatite content and distribution in organic–rich particles. Miner. Eng. 170, 107049.
Manno, C., Stowasser, G., Enderlein, P., Fielding, S., Tarling, G.A., 2015. The contribution of zooplankton faecal pellets to deep–carbon transport in the Scotia Sea (Southern Ocean). Biogeosciences 12, 1955–1965.
Martin, J.H., Knauer, G.A., Karl, D.M., Broenkow, W.W., 1987. VERTEX: carbon cycling in the Northeast Pacific. Deep Sea Res. Part I 34, 267–285.
Mastalerz, M., Schimmelmann, A., Drobniak, A., Chen, Y., 2013. Porosity of Devonian and Mississippian New Albany Shale across a maturation gradient: insights from organic petrology, gas adsorption, and mercury intrusion. Am. Assoc. Pet. Geol. Bull. 97, 1621–1643.
Mastalerz, M., Drobniak, A., Stankiewicz, A.B., 2018. Origin, properties, and implications of solid bitumen in source–rock reservoirs: a review. Int. J. Coal Geol. 195, 14–36.
Minisini, D., Simo, T., Macquaker, J.H., Rudnicki, M.D., 2025. Controls on storage capacity in mudstones. Cementation before sediment compaction and preservation of porosity in lithified rock. Mar. Pet. Geol. 177, 107350.
Morga, R., Wrzalik, R., 2025. Nanoporosity of graptolite periderm by atomic force microscopy (AFM): a case study from the Baltic Basin, Poland. Int. J. Coal Geol. 307, 104816.
Nie, H., Jin, Z., Sun, C., He, Z., Liu, G., Liu, Q., 2019. Organic matter types of the Wufeng and Longmaxi Formations in the Sichuan Basin, South China: implications for the formation of organic matter pores. Energy Fuel 33, 8076–8100.
Ougier-Simonin, A., Renard, F., Boehm, C., Vidal-Gilbert, S., 2016. Microfracturing and microporosity in shales. Earth-Sci. Rev. 162, 198–226.
Pang, Q., Hu, G., Jiao, K., Tan, X., Liu, H., Ye, Y., Yan, S., Zhao, D., 2018. Characteristics of organic pores and composition of bio-precursors in the Wufeng and Longmaxi Formation shales, Southern Sichuan Basin, China. Energy Explor. Exploit. 36, 645–664.
Pang, Q., Hu, G., Hu, C., Zhang, C., 2021. Variation of organic pore structure with maceral types in the Longmaxi Shale, Sichuan Basin. Front. Earth Sci. 9, 715278.
Peng, S., Marone, F., Dultz, S., 2014. Resolution effect in X–ray microcomputed tomography imaging and small pore's contribution to permeability for a Berea sandstone. J. Hydrol. 510, 403–411.
Poulsen, L.K., Iversen, M.H., 2008. Degradation of copepod fecal pellets: key role of protozooplankton. Mar. Ecol. Prog. Ser. 367, 1–13.
Qiu, Z., Liu, B., Lu, B., Shi, Z., Li, Z., 2022. Mineralogical and petrographic characteristics of the Ordovician–Silurian Wufeng–Longmaxi Shale in the Sichuan Basin and implications for depositional conditions and diagenesis of black shales. Mar. Pet. Geol. 135, 105428.
Reed, R.M., Loucks, R.G., Ko, L.T., 2020. Scanning electron microscopy petrographic differentiation among different types of pores associated with organic matter in mudrocks. GCAGS J. 9, 17–27.
Shao, D., Zhang, T., Milliken, K.L., Zhou, S., Li, J., Li, Y., Zhou, Q., 2025. Evolution of a microfracture network induced by hydrocarbon generation during experimental maturation of organic-rich lacustrine shale. Geology 53, 737–742.
Shi, W., Wang, X., Wang, Z., Shi, Y., Feng, A., Chen, N., 2020. A study on the relationship between graptolites and shale gas enrichment in the Wufeng–Longmaxi Formations of the Middle–Upper Yangtze region in China. Arab. J. Geosci. 13, 483.
Simon, M., Grossart, H.P., Schweitzer, B., Ploug, H., 2002. Microbial ecology of organic aggregates in aquatic ecosystems. Aquat. Microb. Ecol. 28, 175–211.

Sing, K.S., 1985. Reporting physisorption data for gas/solid systems with special reference to the determination of surface area and porosity (Recommendations 1984). Pure Appl. Chem. 57, 603–619.
Slatt, R.M., O'Brien, N.R., 2011. Pore types in the Barnett and Woodford gas shales: contribution to understanding gas storage and migration pathways in fine–grained rocks. Am. Assoc. Pet. Geol. Bull. 95, 2017–2030.
Steinberg, D.K., Landry, M.R., 2017. Zooplankton and the ocean carbon cycle. Annu. Rev. Mar. Sci. 9, 413–444.
Su, W., Huff, W.D., Ettensohn, F.R., Liu, X., Zhang, J.E., Li, Z., 2009. K–bentonite, black shale and ffysch successions at the Ordovician–Silurian transition, South China: possible sedimentary responses to the accretion of Cathaysia to the Yangtze Block and its implications for the evolution of Gondwana. Gondwana Res. 15, 111–130.
Sun, L., Wen, Z., He, G., Zhang, P., Wu, C., Zhang, L., Xi, Y., Li, B., 2024. Characteristics of microscopic pore heterogeneity and development model of Wufeng–Longmaxi shales in the Pengshui area of south-east Chongqing. Front. Earth Sci. 18, 188–203.
Tang, L., Song, Y., Jiang, S., Jiang, Z., Li, Z., Yang, Y., Xiao, L., 2020. Organic matter accumulation of the Wufeng-Longmaxi shales in southern Sichuan Basin: evidence and insight from volcanism. Mar. Pet. Geol. 120, 104564.
Tang, X., Jiang, Z., Jiang, S., Wang, H., He, Z., Feng, J., 2021. Structure, burial, and gas accumulation mechanisms of lower Silurian Longmaxi Formation shale gas reservoirs in the Sichuan Basin (China) and its periphery. Am. Assoc. Pet. Geol. Bull. 105, 2425–2447.
Teichmüller, M., 1978. Nachweis von Graptolithen-Periderm in geschieferten Gesteinen mit Hilfe kohlenpetrologischer Methoden. Neues Jahrb. Geol. Paläontol. Monatsh. 1978, 430–447.
Teng, J., Liu, B., Mastalerz, M., Schieber, J., 2022. Origin of organic matter and organic pores in the overmature Ordovician–Silurian Wufeng–Longmaxi Shale of the Sichuan Basin, China. Int. J. Coal Geol. 253, 103970.
Turner, J.T., 2002. Zooplankton fecal pellets, marine snow and sinking phytoplankton blooms. Aquat. Microb. Ecol. 27, 57–102.
Turner, J.T., 2015. Zooplankton fecal pellets, marine snow, phytodetritus and the ocean's biological pump. Prog. Oceanogr. 130, 205–248.
Waliczek, M., Machowski, G., Więcław, D., Konon, A., Wandycz, P., 2019. Properties of solid bitumen and other organic matter from Oligocene shales of the Fore-Magura Unit in Polish Outer Carpathians: microscopic and geochemical approach. Int. J. Coal Geol. 210, 103206.
Wang, Y., Cheng, H., 2023. Advances in microscopic pore structure characterization of fine–grained mudrocks. Energy Fuel 37, 1495–1510.
Wang, Y., Jin, Z., 2019. Effect of pore size distribution on hydrocarbon mixtures adsorption in shale nanoporous media from engineering density functional theory. Fuel 254, 115650.
Wang, Y., Qiu, N., Ma, Z., Ning, C., Zheng, L., et al., 2020. Evaluation of equivalent relationship between vitrinite reflectance and solid bitumen reflectance. J. China Univ. Min. Technol. 49, 563–575.
Wang, Z., Xie, X., Wen, Z., Xu, Y., Liu, Y., 2022. The analysis of bio-precursor organic matter compositions and its significance for gas shale reservoir of Wufeng–Longmaxi Formation from Dingshan area, Sichuan Basin. Minerals 12, 1176.
Wang, J., Ye, F., Lash, G.G., Xi, Z., 2023. Organic matter of the Wufeng–Longmaxi formation shales using scanning electron microscopy. Sustainability 15, 13438.
Wang, Y., Yan, D., Liu, B., Fu, H., Jiang, Q., Yuan, Y., Tian, H., 2025. Organic petrology and geochemistry of the Upper Ordovician–Lower Silurian Renhqiao Formation shales of the Baoshan Block, western Yunnan, China. Int. J. Coal Sci. Technol. 12, 49.
Wei, L., Sun, S., Dong, D., Shi, Z., Yin, J., Zhang, S., Mastalerz, M., Cheng, X., 2021. Petrographic characterization and maceral controls on porosity in overmature marine shales: examples from Ordovician–Silurian shales in China and the U.S. Geofluids 2021, 5582262.
Wu, L., Lu, Y., Liu, X., He, G., 2018. Effects of volcanic activities in Ordovician Wufeng–Silurian Longmaxi period on organic-rich shale in the Upper Yangtze area, South China. Pet. Explor. Dev. 45, 862–872.
Wu, J., Liang, C., Hu, Z., Yang, R., Xie, J., Wang, R., Zhao, J., 2019. Sedimentation mechanisms and enrichment of organic matter in the Ordovician Wufeng Formation–Silurian Longmaxi Formation in the Sichuan Basin. Mar. Pet. Geol. 101, 556–565.
Wu, J., Luo, Q., Zhong, N., Goodarzi, F., Bai, Y., Suchý, V., et al., 2025. The organic petrology of graptolites in sections parallel and perpendicular to the bedding: Implication for thermal maturity evaluation. Int. J. Coal Geol. 310, 104883.
Xie, G., Hao, W., 2022. Identifying organic matter (OM) types and characterizing OM pores in the Wufeng–Longmaxi shales. ACS Omega 7, 38811–38824.
Xu, C., Yao, S., Song, D., Liu, Y., 2020. Types, chemical and porosity characteristics of hydrocarbon–generating organisms of the lower Paleozoic, south China–Taking Longmaxi Formation and Qiongzhusi Formation in Sichuan Basin as examples. Mar. Pet. Geol. 119, 104508.
Zargari, S., Canter, K.L., Prasad, M., 2015. Porosity evolution in oil–prone source rocks. Fuel 153, 110–117.
Zhang, Y., He, Z., Lu, S., Jiang, S., Xiao, D., Long, S., et al., 2020. Characteristics of microorganisms and origin of organic matter in Wufeng Formation and Longmaxi Formation in Sichuan Basin, South China. Mar. Pet. Geol. 111, 363–374.
Zhu, H., Huang, C., Ju, Y., Bu, H., Li, X., Yang, M., et al., 2021. Multi–scale multi–dimensional characterization of clay–hosted pore networks of shale using FIBSEM, TEM, and X–ray micro–tomography: Implications for methane storage and migration. Appl. Clay Sci. 213, 106239.
Zou, C., Dong, D., Wang, Y., Li, X., Huang, J., Wang, S., et al., 2015. Shale gas in China: characteristics, challenges and prospects (I). Pet. Explor. Dev. 42, 753–767.